# Shallow Bathymetric Mapping via Multistop Single Photoelectron Sensitivity Laser Ranging

Kristofer Y. Shrestha, *Member, IEEE*, William E. Carter,
K. Clint Slatton, *Senior Member, IEEE*, and Tristan K. Cossio, *Member, IEEE*

***Abstract*—We discuss the optimization of components in a single-wavelength airborne laser bathymeter that is intended for a low-power unmanned aerial vehicle platform. The theoretical minimum energy requirement to detect the submerged sea floor in shallow ($< 5$ m) water using a low signal-to-noise ratio (LSNR) detection methodology is calculated. Results are presented from tests of a prototype light detection and ranging (LiDAR) instrument that was developed by the University of Florida, Gainesville. A green wavelength (532 nm), 100-beamlet, low-energy (35-nJ/beamlet), short-pulse (480 ps) laser ranging system was operated from a low-altitude (500-m) aircraft, with a multichannel sensor that is capable of single photoelectron sensitivity and multiple stops. Data that were collected during tests display vertical structure in shallow-water areas based on fixed threshold crossings at a single-photon sensitivity level. A major concern for the binary detection strategy is the reliable identification and removal of noise events. Potential causes of ranging errors related to photomultiplier tube afterpulsing, impedance mismatching, and gain block overdrive are described. Data collection/processing solutions based on local density estimation are explored. Previous studies on LSNR performance metrics showed that short (15-cm) dead time could be expected in the case of multiple scattering objects, indicating the possibility of seamless topographic/bathymetric mapping with minimal discontinuity at the waterline. LiDAR depth estimates from airborne profiles are compared to on-site measurements, and near-shore submerged feature identification is presented.**

***Index Terms*—Airborne laser swath mapping (ALSM), bathymetry, light detection and ranging (LiDAR), photonics.**

Manuscript received February 18, 2011; revised October 14, 2011 and January 12, 2012; accepted March 11, 2012. Date of publication May 21, 2012; date of current version October 24, 2012. This work was supported in part by the Office of Naval Research under Grant N00014-04-0365.

K. Y. Shrestha was with the Department of Civil and Coastal Engineering, University of Florida, Gainesville, FL 32611 USA. He is now with the Department of Earth and Atmospheric Sciences, Georgia Institute of Technology, Atlanta, GA 30318 USA (e-mail: kshres@gmail.com).

W. E. Carter was with the Department of Civil and Coastal Engineering, University of Florida, Gainesville, FL 32611 USA. He is now with the Department of Civil and Environmental Engineering, University of Houston, Houston, TX 77004 USA, and also with the National Center for Airborne Laser Mapping, National Science Foundation, Houston, TX 77204 USA.

K. C. Slatton, deceased, was with the Department of Electrical and Computer Engineering, University of Florida (UF), Gainesville, FL 32611 USA.

T. K. Cossio was with the Department of Electrical and Computer Engineering, University of Florida, Gainesville, FL 32611 USA. He is now with the Johns Hopkins University Applied Physics Laboratory, Johns Hopkins University, Baltimore, MD 21287 USA.

Color versions of one or more of the figures in this paper are available online at http://ieeexplore.ieee.org.

Digital Object Identifier 10.1109/TGRS.2012.2192445

## I. Introduction

### A. ALB Background

THE ABILITY of light detection and ranging (LiDAR) hydrography to create detailed maps through flexible data collection methods supports a variety of applications, including nautical charting, hazard identification, erosion modeling, storm damage assessment, and beach nourishment/design [1]. In 1973, a joint program for constructing an operational airborne laser bathymetry (ALB) unit was founded by the National Aeronautics and Space Administration (NASA) Wallops Flight Center LiDAR Research Group and the U.S. Naval Oceanographic Office, resulting in test flights from 1973 to 1975 [2]. By the late 1980s, the idea of ALB showed promise from systems such as the NASA Airborne Oceanographic LiDAR (AOL), the Canadian Larsen 500, the Australian WRELADS, and the Swedish FLASH [3]. Operational systems matured during the early part of the next decade, with successes by systems such as the Royal Australian Navy's Laser Airborne Depth Sounder (LADS), the U.S. Army Corps of Engineers' Scanning Hydrographic Operational Airborne Laser Survey (SHOALS), and the Swedish Maritime Administration's HawkEye. As the volume of data and rate of acquisition became less challenging with improving computer technology, the processing workflow moved from a manually intensive line-based approach to an automatic area-based methodology [1]. Through the early 2000s, continued improvements have been made to increase the pulse rate, spot spacing, and portability of ALB systems [4]–[6], but the nature of submerged sensing—the measurement of the water column and bottom through elastic backscatter measurements at (green) wavelengths of 500–550 nm—remains largely the same.

ALB systems are currently routinely flown on light aircraft platforms ($< 5670$ kg) such as the de Havilland Canada (DHC) Twin Otter. In this paper, we will consider the possibility of integrating a sensor package onto an even smaller aircraft—an unmanned aerial vehicle (UAV). Introducing a large heavy payload may impede flight operations for this type of platform. Considering that ALB designs with a high signal-to-noise ratio (HSNR) often favor simplified detection over weight, size, and power consumption [7], [8], it is of interest to consider the minimum requirements for shallow bathymetry mapping, i.e., the parts of the ALB process that can be optimized in the context of technology improvements. Utilizing a high-energy laser can shorten the mission duration by draining the battery life; high-power lasers require complex electronics and sophisticated cooling systems. Bulky equipment is unsuitable

for scalability with low-power applications. Replacement costs may also carry more significance. UAVs are often intended for potentially "disposable" functions, and the loss of an expensive laser mapping unit can be prohibitive. Operation in populated areas restricts maximum laser power and sensor altitude due to eye safety requirements. Designs based on a high energy requirement per illuminated area limit the size of the footprint, resulting in less than contiguous coverage of the terrain. We can suggest the following three areas in which to optimize ALB components to prepare for a low-power platform: 1) output wavelength; 2) output energy; and 3) waveform capture.

### B. Output Wavelength

In a typical ALB system, a 532-nm (green) laser is mandatory due to its water penetration capabilities. The emission of 1064-nm (infrared) radiation is useful for identifying the water surface and for mixed topographic mapping [9]–[12]. In addition, a receiver that can sense the 645-nm (red) wavelength in conjunction with parallel green waveforms can be beneficial for distinguishing the specular interface reflection from the diffuse bottom reflection. The excitation of water molecules at the water surface by the green laser energy or induced vibrational modes of the O–H stretch in liquid water causes energy to be reemitted as photons at a different wavelengths (Raman scattering) [11]. Based on these ideas, data from the Optech SHOALS have been used to make high-density measurements of the coastal zone for a number of years [10]. This system is sensitive to bottom returns out to two to three times the Secchi depth and to a maximum of 60 m in the clearest coastal waters. Recent developments in sensor design have shown that we may eliminate the dependency on infrared transmission and the red-channel receiver with new sensor configurations. The air–water interface reflectivity in the green spectrum is often subject to significant variation dependent on environment conditions [13], but creative methods can be employed to overcome potential pitfalls. One example is shown in the next section.

Sensors that are intended to provide green-waveform submerged sensing must typically be optimized for deep-water applications; the exponential decay in signal strength through the water column necessitates large amplification at the receiver. With such large-amplification techniques, strong signals that result from the air–water interface may saturate the detector. This condition is one of the reasons that a multiple-receiver/multiple-wavelength approach is traditionally used for ALB. Data that are collected by the NASA Experimental Advanced Airborne Research LiDAR (EAARL) has indicated the potential for single-wavelength (green) laser backscatter measurement in the surveying of shallow submarine topography. Building on the progress of topographic LiDARs that were engineered to sense the vertical structure of vegetation canopies, the EAARL employs a frequency-doubled neodymium-doped yttrium aluminum garnet (Nd–YAG) laser that produces 10-kHz, 1.3-ns-duration, 70-$\mu$J pulses along with four 1-ns temporal waveform digitizers. The parallel operation of the four digitizers in the EAARL system compensates for saturation issues. Optical rugosity analysis in Biscayne National Park showed measurements that were consistent with field observations of coral features relative to rubble-dominated bank reefs within the study area out to 12-m depths [14]. EAARL data have indicated that green-only laser bathymetry is a viable alternative.

### C. Output Energy

The EAARL presents an interesting new option for small-footprint ALB, but the system nominally outputs more than 50 $\mu$J of output energy per laser pulse. In this paper, we will consider this level to be "high energy," because we are interested in exploring the minimum requirements for shallow benthic detection. In theory, surface mapping efficiency can significantly be improved by using a paradigm with a low signal-to-noise ratio (LSNR) based on lower energy and shorter pulse lasers [8], [15]. LSNR LiDAR has been demonstrated to work well for low-noise environments such as satellite laser ranging [16], [17], but shallow-water bathymetry presents a host of new variables with which to contend due to a considerably more noisy environment. The application of these ideas is not nearly as common for ALB. Traditional ALB often relies on HSNR detection, because it ensures the separation of true return signals from sources of spurious noise events such as atmospheric scattering and detector dark noise. The extension of low-noise satellite ranging theory for use in airborne LSNR ALB will be detailed in Section II. Both HSNR and LSNR methods may still contain erroneous points that are associated with multipath (sequential reflections from different surfaces prior to returning to the sensor).

If a system can function using a low-output-energy source ($<$ 100 nJ), we can take some liberties with system design that were not previously possible. For example, the new power requirements allow us to holographically divide the beam of a low-power microlaser ($< 5$ $\mu$J) into an array of subbeamlets and pair it with a high-gain ($> 10^4$) photomultiplier tube (PMT) that can distinguish independent responses over a grid [18]. The spatial resolution then becomes a function of the array size. Denser point spacing may help offset ambiguity in feature identification, which is likely to be a problem when operating near the noise floor. For LSNR ALB, this approach means evaluating depths as measurements between an interpolated interface and a submerged surface and necessitates 3-D post-processing that is reliant on the local coherence of reflecting features. Even with beam-splitting operations, the capability of detecting returns at very low output energy allows the use of small-form-factor ($< 40 \times 15 \times 15$ cm) microlasers.

### D. Waveform Capture

Traditionally, ALB systems have recorded a digitization of the return waveform that results from each laser shot (often referred to as "full-waveform ALB"). Employing high digitization resolution allows for the reconstruction of a near-continuous height profile related to the interface, water column, and bottom. A postprocessing algorithm can identify inflection points in the reconstructed signal associated with these features. Small-footprint LiDARs then provide detailed characterization of vertical structure at high spatial resolution [19]. For full-waveform ALB, the interface-component signal amplitudes strongly depend on the beam nadir angle, wind speed, and

specific irradiated wave slopes, causing surface signals to vary across a large dynamic range [20]. The resulting surface uncertainty problem is an issue for system designers who attempt to decide which portions of the return waveform to interpret as sea surface and bottom in a real-time automatic manner.

Assuming no saturation (waveform clipping), one way of addressing the dynamic range issue is by modifying calculations of range based on signal shapes and amplitudes. Given that modern systems routinely receive thousands of these signals per second, integrated processing procedures are commonly implemented. For example, ranges that are derived from very large amplitude signals that irregularly occur may need corrections for expected timing offsets (range walk). In waveform digitization postprocessing or embedded filtering (such as constant-fraction discrimination), noise observations are automatically detected and discarded to reduce the overall data set size. Outcomes such as amplitude dependent range walk, slope dependency of range, and signal ringing can have negative effects without proper compensation [21]. The same problems apply for LSNR ranging.

It is an interesting proposition, therefore, to consider how relative accuracies from a simple fixed-threshold detection strategy for LSNR detection, resulting in a binary data structure, may compare to accuracies from full-waveform LiDAR. A threshold must be set corresponding to a single-photon sensitivity level due to the low-energy output. The detection of a photon then results in a threshold crossing or a "1" data entry for a given range bin. If no laser backscatter is present to activate the detector during the range bin interval, a "0" data entry is recorded. Range is calculated by differencing the time at which the laser pulse exits the aircraft and the next time at which a "1" is registered at the receiver. Using this simplified approach, there is only 1 bit for each time step through which to discriminate an inflection point from the return pulse; in comparison, traditional waveform systems often employ 8-bit digitization or larger.

The binary method offers certain advantages. Instead of attempting to work with a multitude of photons and providing estimates for optical power integration, the system effectively records all observations without having to resort to an interpretive algorithm. A serious disadvantage, however, is the increased probability of false positives when extracting true signals from background noise [7]. Daytime operation can cause an increase in solar events, which may be misclassified as surface returns because of the simplified binary structure. Noise must be kept to a minimum at high amplification through careful selection of spatial, spectral, and temporal filters [19].

In addition, it is imperative that the ranging system have extended multistop capability with a high-speed receiver and employ short outgoing laser pulsewidth. First-stop systems record only data that are associated with the first target that was encountered by the laser pulse. A timing system is capable of "multiple stops" if it can record multiple returns (stops) beyond the initial triggered response. It follows that, because the LSNR paradigm may be faced with significant solar/dark noise, multistop capability is essential. "Dead" or recovery time is a significant factor for multistop systems; in the case of partial reflections for distributed targets, the receiver should recover faster than the timing bin resolution. Utilizing a short pulsewidth—a good rule of thumb is to use a width smaller than the timing bin resolution—helps ensure that multiple binary events are unique, but pulse stretching and high-amplitude decay remain relevant. Even with multistop capability and a short pulsewidth, the effect of noise on data will be the central concern for this type of simplified structure.

### *E. University of Florida LSNR ALB Prototype*

The goal of this paper is to explore the viability of mixed topographic and shallow bathymetric ($< 5$ m) mapping through a low-altitude ($< 600$ m), single-wavelength (532-nm), low-energy ($< 50$ nJ), short-pulse ($< 1$ ns) laser ranging system that operates with the aforementioned optimizations. Recorded depths should conform to International Hydrographic Organization (IHO) Order 1 accuracy standards ($\pm 50$ cm in a 5-m depth at a 95% confidence interval). A prototype LSNR system, the Coastal Area Tactical-Mapping System (CATS), has been developed by the University of Florida for this purpose. In Section II, we detail the theoretical justification for the design. Section III addresses the ranging capabilities and airborne testing of the prototype. Section IV discusses data processing, and Section V analyzes airborne bathymetry data. Section VI presents conclusions and suggestions for future work.

## II. THEORY

### *A. LSNR LiDAR Background*

At 532 nm in a typical coastal environment, less than 2% [13] of the laser light is reflected back from the air–surface interface. The following two primary losses should be considered as laser light propagates through the water column: 1) absorption and 2) scattering. These losses can be described by the spectral absorption and scattering coefficients $a_\lambda$ and $b_\lambda$, respectively. The sum of these two quantities is the total beam attenuation coefficient $c_\lambda$ [22]. At the interface, a large portion of the green laser pulse is refracted into the water column. The beam undergoes scattering from entrained microscopic particulates. A fraction of the transmitted energy in the water column, which exponentially decreases in magnitude with greater depth, is incident on the bottom, with a lateral extent that depends on the scattering properties of the medium and optical depth. A general expression for signal energy that propagates a distance $R_w$ in the water medium is [7]

$$E(R_w) = E_0 * \exp(-c_\lambda R_w). \tag{1}$$

A portion of this incident energy, typically 4%–15%, depending on the bottom composition [11], is reflected from the sea floor back into the water column. Absorption and scattering again, respectively, attenuate and stretch the pulse as it passes back to the surface, where it is refracted back into the atmosphere.

The reduction in signal strength as the laser light propagates through the water column motivates a significant increase in the transmitted energy per pulse to range to greater depths. The generation of large amplitude pulses ($> 2$ mJ) in past systems resulted in typical outgoing pulsewidths of $> 10$ ns,

which, in turn, reduced the capability of typical ALB systems to accurately survey shallow ($<$ 5 m) coastal areas [6], [11]. As laser technology continues to evolve, high ($>$ 1 mJ) output energies at short (1–5 ns) pulsewidths are becoming more cost effective. The use of "short-pulse" LiDAR systems can help reduce complications in mixed-waveform processing [23].

In addition to requiring fairly sophisticated lasers, outputting high pulse energy can raise eye safety issues at low altitudes. Because low-altitude ($<$ 500 m) applications can potentially provide higher point density, it is of interest to consider the limits for low-power detection. Traditional HSNR designs do not make the most efficient use of available photons, because they favor simplified detection over other system aspects, for example, size, weight, and power consumption [8]. In HSNR designs, the green beam is usually expanded to a diameter of a few meters at the water surface to achieve eye-safe operation [24]. This approach is unnecessary if a much lower power laser is used. Theoretical analysis that was carried out based on a multiple-forward scattering and single-backscattering model for narrow field-of-view LiDAR return signals indicated an increase in bottom definition, enhancement in depth measurement accuracy, reduction of post-surface return effects in the PMT, and greatly improved rejection of ambient light, permitting operations in all zenith sun angles and flight directions [25]. Given that producing low-power ($< 5\ \mu$J) pulses in short duration ($<$ 1 ns) is easier, we can also expect the required components to be less expensive. Changing from a traditional HSNR approach to LSNR requires a high-sensitivity detector.

Moving to an LSNR detection paradigm can successfully pair highly sensitive photodetectors such as the microchannel plate photomultiplier tube (MCP-PMT) with cost-effective low-power microchip lasers to achieve mixed-feature mapping [15], [19], [26], [27]. A photodetector such as the avalanche photodiode (APD) or PMT needs to employ substantial amplification ($> 10^4$) to magnify low amounts of this backscattered energy ($<$ 1 fJ or $< 2.675 \cdot 10^3$ photons at 532 nm) into a measurable signal. Detection beyond 10-m depths in current systems has typically required more significant outgoing pulse energy at 532 nm ($> 50\ \mu$J) [14]. To calculate the minimum output energy that is required for single-photon detection in our case, the signal strength should be estimated as a function of transmitter, receiver, and environment characteristics. The uncertainty of an observation can be measured as a function of the various errors sources [28]. Even for a radiation field of constant intensity, the number of photons that arrive at the photodetector for a given time interval is inherently uncertain due to the discrete nature of the incident light, charge carriers, and the interaction of light with the photodetector [29]. Statistical proofs show that, if photon arrival rates are time independent (which means that they can be described as being a statistically stationary process), the total number of photons that arrive during any time interval is Poisson distributed [30]. The relationship between the number of photons incident on the detector and the number of emitted photoelectrons (p.e.) can then be expressed as the following probability:

$$P(n_t, n_s) = n_s^{n_t} \cdot \frac{e^{-n_s}}{n_t!} \tag{2}$$

TABLE I
SAMPLE SYSTEM PARAMETERS FOR LIDAR LINK EQUATIONS

| | |
|---|---|
| $n_h$ | 0.8 |
| $n_q$ | 0.28 |
| $n_r$ | 0.4 |
| $h$ | $6.63 \cdot 10^{-34}$ J·s |
| $v$ | $5.64 \cdot 10^{14}$ Hz |
| $\rho_\lambda$ | 0.15 |
| $a$ | 5° |
| $A_r$ | $3.3 \cdot 10^{-3}$ m$^2$ |
| $B_{e,\lambda}$ | $0.297 \cdot 10^{-3}$ m$^{-1}$ |
| $R$ | 600 m |
| $a_t$ | 3.5° |
| $R_{air}$ | 600 m |
| $R_w$ | 5 m |
| $a_s$ | 5° |
| $a_r$ | 3.76° |
| $r_{\text{int}}$ | 0.01 |
| $a_{\lambda,pure}$ | 0.0517 m$^{-1}$ |
| $b_{\lambda,pure}$ | 0.0025 m$^{-1}$ |
| $a_{\lambda,coastal}$ | 0.1790 m$^{-1}$ |
| $b_{\lambda,coastal}$ | 0.2190 m$^{-1}$ |

where $n_t$ is the expected number of detected PEs, and $n_s$ is the expected number of PEs that were generated at the receiver. The probability of registering at least one signal event can then be calculated as a function of $n_s$ [7]. For example, it is expected that, for a signal level of one PE, there is a 63.21% chance that a signal event will be registered. The LiDAR link equation relates basic elements to estimate the backscattered signal strength. A modified form of this equation yields the following expression for transmitted energy per laser pulse in the topographic case [15]:

$$E_{t,topo} = \frac{hv \cdot n_s}{n_h n_q n_r \cdot \rho_\lambda \cdot \cos(\alpha) \cdot \frac{A_r}{\pi R^2} \left[\exp(-\beta_{e\lambda} R)\right]^2} \tag{3}$$

where $h$ is Planck's constant, $v$ is the photon frequency, $n_h$ is the hologram (in the case of an altered beam) efficiency, $n_q$ is the detector quantum efficiency, $n_r$ is the receiver optical efficiency, $\rho_\lambda$ is the wavelength-dependent surface coefficient, $\alpha$ is the local incidence angle on the surface, $A_r$ is the collecting area of the receiver aperture, $R$ is the range to the surface, and $\beta_{e,\lambda}$ is the atmospheric extinction coefficient per meter. Table I shows sample system parameters for moderate laser output power, modest telescope aperture, and average efficiencies for commercially available materials. The sample values indicate that we expect 20% transmission loss from the hologram that creates the beamlet array, 28% quantum efficiency in the detector, 60% loss due to spatial and spectral filters, 15%

reflectivity for typical ground soil at 532 nm, a 6.5-cm-diameter telescope, and a 600-m flying height. To have a 63.21% chance of detecting one signal event with these parameters, the transmitted energy $E_t$ should be larger than 13.5 nJ for each beamlet. For a hologram that projects 100 beamlets, we should use a laser that outputs more than 1.35 $\mu$J of the total energy.

For the submerged case, we assume that single scattering will dominate the received signal due to the small-spot radius that is viewed by the receiver [31] and therefore ignore multiple scattering effects. The expression for transmitted energy in (3) is modified by including water column extinction parameters as

$$E_{t,bathy} = \frac{hv \cdot n_s}{n_h n_q n_r \cdot \rho_\lambda \cdot \cos(\alpha_t) \cdot \frac{A_r}{\pi(R_{air}+R_w)^2}} \cdot \frac{1}{\left[1 - r_{\text{int}}(\alpha_s)\right]^2 \cdot \left[\exp(-\beta_{e\lambda} R_{air})\right]^2 \cdot \left[\exp(-c_\lambda R_w)\right]^2} \quad (4)$$

where $\alpha_t$ is the incidence angle to the ocean bottom, $R_{air}$ is the range in air to the water surface, $R_w$ is the range in water to the bottom, $\alpha_s$ is the angle of incidence to the mean ocean surface, $\alpha_r$ is the refracted angle in the water medium given by Snell's law, and $r_{\text{int}}$ is the reflectance coefficient at the air–water interface. If we consider further practical values (also given in Table I) for near-nadir bathymetric ranging with "pure-sea-water" absorption $(a_{\lambda,pure})$ and scattering $(b_{\lambda,pure})$ coefficients, we find that a 5-m depth requires at least 24.3 nJ of transmitted energy. Inputting more realistic values for the "coastal" water case $(a_{\lambda,coastal}, b_{\lambda,coastal})$ yields a threshold of 0.76 $\mu$J. Further discussion of the derived equations, noise components, and simulated performance metrics can be found in [7] and [32].

## III. Prototype Testing

### A. Ranging Capability Assessment

We are interested in a practical assessment of these theoretical assertions. Analysis of range data from the CATS prototype is shown here. A frequency-doubled Nd:YAG laser is used to create 532-nm, 3.5-$\mu$J pulses at 8 kHz. The division of the primary beam into an evenly spaced array (10 × 10) of 35-nJ beamlets creates dense spot spacing (∼20 cm) at a flying height of 600 m. Additional device specifications and parameters necessary for precise temporal, spatial, and spectral filtering were described in a previous work [19]. We now present a ranging capability assessment based on static experiments.

*1) Range Accuracy:* A calibration test was conducted to evaluate the consistency of returns from a fixed target. The CATS was set up to range to a brick wall under full solar illumination on a clear day. For 16 000 laser shots (approximately two seconds of laser-on time), 1 279 197 total hits were recorded. Hits were filtered for returns from 264 m to 266 m to discard any dark noise or solar events that are not associated with scattering off the brick. We considered 72% of these hits (922 202 points) to evaluate relative accuracy. An associated histogram of range information is shown in Fig. 1. At one standard deviation from the mean, 99% of the recorded range data falls within the 10–20 cm level, as shown in Fig. 2. The outlier at channel 33 only registered six hits, which is a very small sample (0.07%) in relation to other channels. This channel was designated inoperable due to low sensitivity.

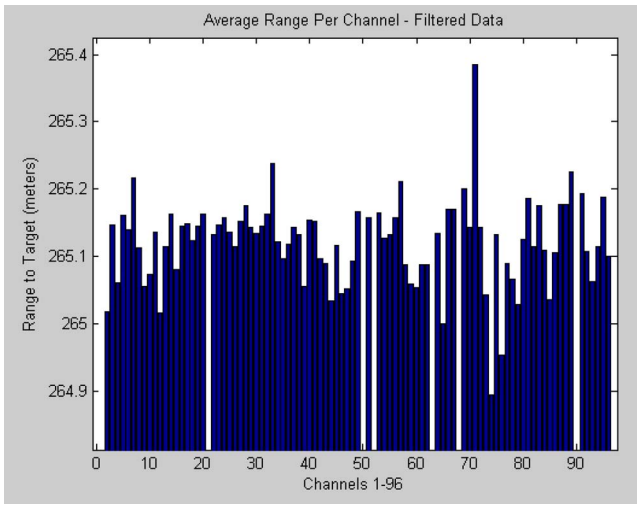


Fig. 1. Histogram of the average range per channel in the static (no-scan) test.

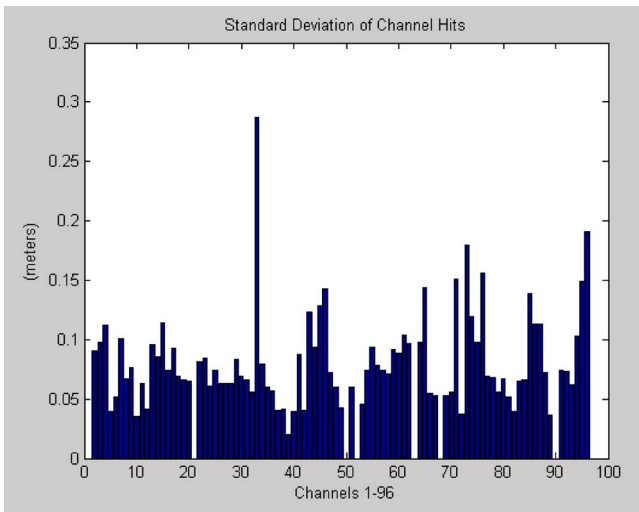


Fig. 2. Standard deviation of recorded ranges per channel in the static (no-scan) test.

*2) Minimum Separation Distance, Bathymetric Mapping Depth, and Atmospheric Scattering:* Performance metrics were assessed in further static experiments [19] to determine values for minimum separation distance, bathymetric mapping depth, and atmospheric scattering. These results show that a secondary surface intercepted by a partially occluded laser beam can be detected at a distance of 15 cm. Ranges were recorded through water columns of variable depth. At a depth of 50 cm in coastal water, on the average, 12% of laser shots registered at least one signal event. For 20-cm spacing between laser spots, this was estimated to be a sufficient signal level to produce meter-scale shallow (2–5 m depth) bathymetry data [7]. Static testing also established that, for surface–bottom separation in a heavily turbid suspension (7.5-cm visibility), the maximum MCP-PMT gain $(8 \cdot 10^5)$ was necessary to produce adequate discrimination. Employing maximum gain introduced 70 times more noise from atmospheric backscatter relative to a multiphoton state $(2 \cdot 10^5$ gain) on a clear day.

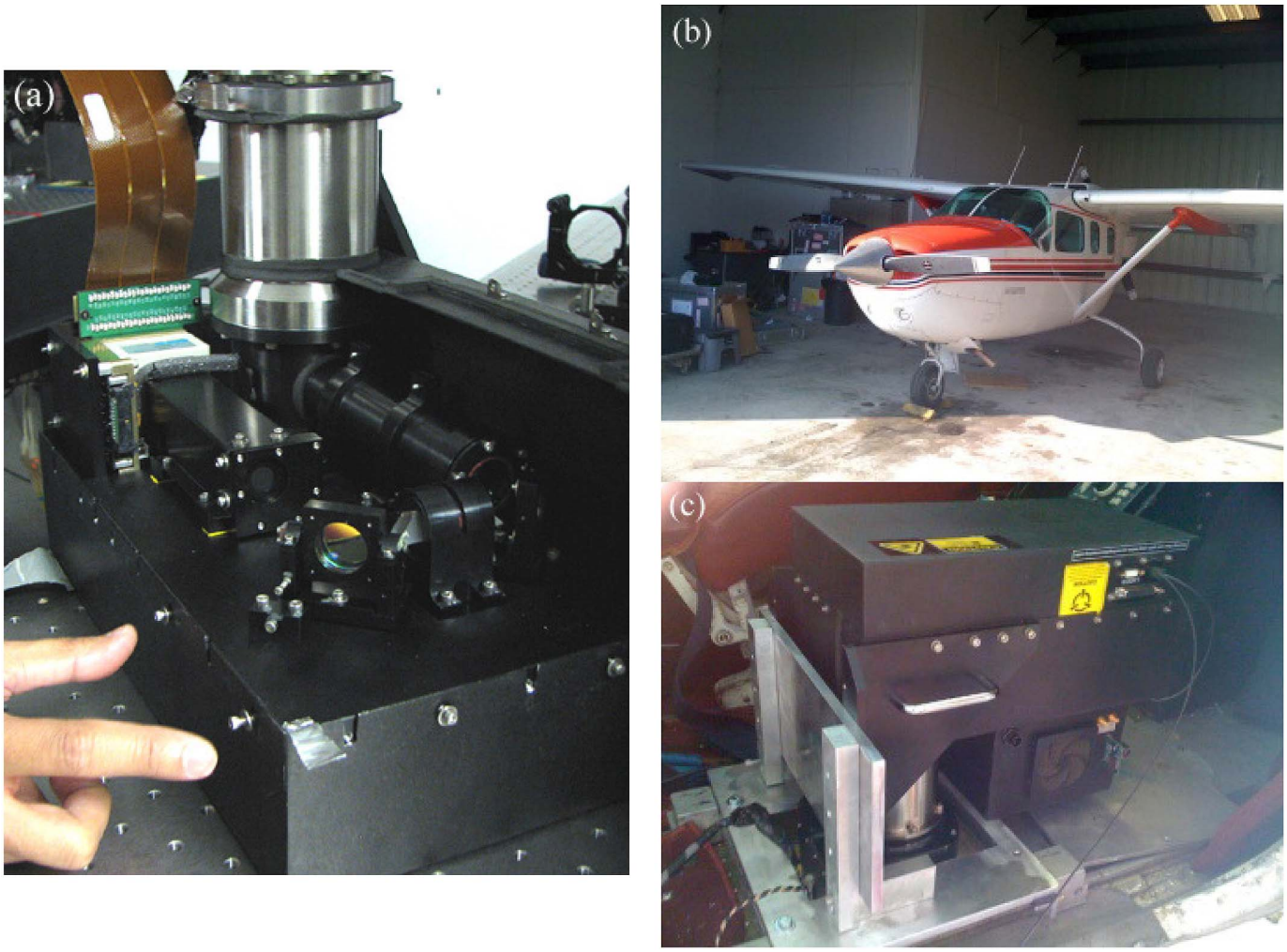


Fig. 3. (a) Received path portion of the optical bench. (b) Cessna Skymaster aircraft. (c) Mounted CATS sensor head.

### B. Airborne Testing of Prototype

*1) Experimental Setup:* The CATS sensor was mounted in a Cessna Skymaster twin-engine aircraft, as shown in Fig. 3. To minimize costs, it contained no inertial measurement unit (IMU). A special mount was constructed out of aluminum plates and directly bolted to the rails that normally support the copilot's seat. The system was therefore rigidly attached to the aircraft frame, but no IMU data were collected with which to correct the observations for changes in the orientation of the aircraft. Artifacts that result from changes in the orientation of the aircraft (roll, pitch, and yaw) include undulations of flat water surfaces and lateral wandering of the surface profiles.

*2) Dynamic Range Observations:* Experiments were conducted to test the system's airborne profiling capability. The two prisms were set 180° out of phase so that the laser was pointed at the nadir. The aircraft was flown at approximately 60-m/s and 500–600 m height above ground level for a series of ranging trials at full PMT amplification over land. Flights were conducted at night to reduce the effect of solar noise. In the aforementioned static testing, employing maximum gain on the PMT produced very large signals over bare-earth surfaces, resulting in data flow difficulties when attempting to record 100 channels of multistop information. To reduce the data throughput, only channels on the second ranging board (17–32 or the central $4 \times 4$ square) were enabled for a majority of the experiments.

The preliminary analysis of data from test flights showed that the overall signal strength at the maximum PMT gain (2500 V or $8 \cdot 10^5$) was high enough to warrant changing data collection parameters. Responses from strongly reflective surfaces at this gain level produced a stacking effect (hits in many consecutive range bins) near roof surfaces in the resulting image. Because the laser output energy and detector type were selected to maximize the LSNR performance in turbid waters, this outcome was expected. The dynamic range between responses from different types of features (particularly when contrasting topographic and bathymetric return) can be large; for example, it is not uncommon to have a difference of more than six orders of magnitude between strong water interface and weak bottom returns [24]. Responses from artificial surfaces for on-nadir beam propagation at 2500 V were tens of range bins deep in some cases. Stacking effects from large-magnitude water surface responses are undesirable, because they can eclipse multiple return data from partial reflections.

*3) Off-Nadir Profiling:* By changing the type of airborne profiling from on nadir to off nadir, we can begin to combat

the dynamic range problem. Although traditional "sawtooth" (raster scan) patterns pass through the nadir in each swath, conical or circular patterns are the natural extension of off-nadir scanning. By imposing a fixed incidence angle relative to the ground for outgoing laser light, the magnitude of backscattered radiation is decreased due to less significant contributions from specular reflections and increased slant range. This condition has special relevance in the case of mirror-like water surfaces, because large specular components may cause problems for on-nadir operation. However, even with off-nadir operation, a large difference in signal strength between topography and distributed targets such as partially occluded forest canopies and submerged surfaces was still observed.

For the LSNR detection paradigm to be worthwhile related to submerged surface mapping, an amplification level that produces returns from even very weak scatterers should be maintained. Data collections at multiphoton sensitivity (2300-V or $2.5 \cdot 10^5$ gain) produced responses that are three to four range bins deep from surfaces such as building roofs, bare earth, and tops of tree canopies. We could thus reduce the tube voltage and expect the top end of our dynamic range to be reduced. Theoretically, if interrogated far-field surfaces are of uniform reflectance and the gain of the tube is matched to provide just enough amplification to consistently produce threshold crossings, this technique might be acceptable. However, in practice, target reflectance properties are not precisely known, and the tailoring detection strategy to one type of feature negates the real benefit of this type of sensor, i.e., mixed mapping. Previous experimentation [19] showed that shallow-water bathymetry is difficult at less than full amplification (2500-V or $8 \cdot 10^5$ gain) for very low output energy ($< 50$ nJ).

## IV. Data Processing

A sensor that was intended to provide seamless near-shore mapping should accommodate difficulties that are associated with the land–water boundary. The NASA EAARL system uses four stages of detectors to combat dynamic range challenges in green-only mapping [14], but the CATS has only a single PMT. The CATS still provides mixed topographic mapping, but 3-D data postprocessing is required. These same topographic processing procedures will be applied to bathymetric data. True signals should exhibit some form of spatial coherence even in lowly populated areas due to the random nature of noise formation, allowing us to use techniques such as postdetection Poisson filtering (PDPF) and a correlation range receiver (CRR) to beneficially exploit data trends [15]. We will consider in detail the most significant type of error specific to the CATS—false surfaces or "ghost images"—to evaluate the applicability of this claim for mixed topographic and bathymetric data processing.

### A. Ghost Images

Several different types of buildings and other man-made objects were profiled in a flight over the University of Florida campus in Gainesville, Florida. Fig. 4(a) shows an aerial photograph of a region at the south end of the campus and flight line. Fig. 4(b) is the raw point data from channels 20 and 23. The image allows us to identify a small outcropping in a building roof, a roof from a nearby parked car, angled roof geometry from small office buildings, the outline of a stone bench, and a low-hanging awning between two buildings. A zoom-in on detected surfaces, as shown in Fig. 4(c), identifies a potential problem: a "ghost image" of roof surfaces appears at a constant offset beyond the first return. These false surfaces need to be eliminated from the data set. For bare-earth and building measurements, removal could be accomplished through an automatic first-surface algorithm, but we then risk losing important multiple-return information from other types of features. Leaving the data unfiltered is similarly unacceptable. In the worst case scenario, an automatic data classifier may erroneously identify a ghost image from the water surface as a submerged element, yielding inaccurate depth estimation. Identifying the cause of such artifacts and addressing their influence on feature classification is of prime importance for shallow-water bathymetry.

The influences of ghost returns are not always obvious, because the magnitudes of the effects are suspected to be fairly low, which means that certain types of data visualizations can cause the effects to be classified as random thermal events, solar noise, or volumetric scattering residuals rather than deterministic occurrences. This case is particularly true when illuminating nonuniform multiple-scattering surfaces. For example, when returns from channel 23 are plotted in Fig. 5, noise trends are less prominent. Here, we show an unfiltered point cloud from a forested region in Mine Run, VA. Small leaf structure elements are definable based on a large number of multiple scattering events. The flight was conducted in autumn, because the deciduous forest was in the process of shedding leaves; this condition left small pockets of space in the overhead canopy through which individual beamlets could propagate. Partial transmission of beam elements as a result of semiocclusion by leaf surfaces allow for intracanopy response and the identification of the ground surface below the tree line. A zoom-in depicting a narrow tree trunk is pictured.

An expanded view of the same near-shore scene is depicted in Fig. 6. Fig. 6(a) shows the first-return data. The resulting point cloud seems close to what we would expect; canopy returns are logically distributed for partial leaf-on conditions, bare-earth surfaces ($\mathrm{x} < 150$ m) are singular, and water returns ($\mathrm{x} > 150$ m) are generally bimodal. The distribution of noise returns relative to these known features, however, should be analyzed in further detail.

### B. Noise Expectations

Above the ground/water surface, we expect random contributions from dark/solar events and atmospheric backscatter. Below ground and past $\sim$5 m water depth, we expect only contributions from dark/solar noise. Fig. 6(a) thus gives us some indication that an aberrant effect may be in play; below ground noise events are more numerous. The opposite should be true if we expect our noise to randomly be distributed. When all returns from 16 channels of data are plotted [Fig. 6(b)], artifacts

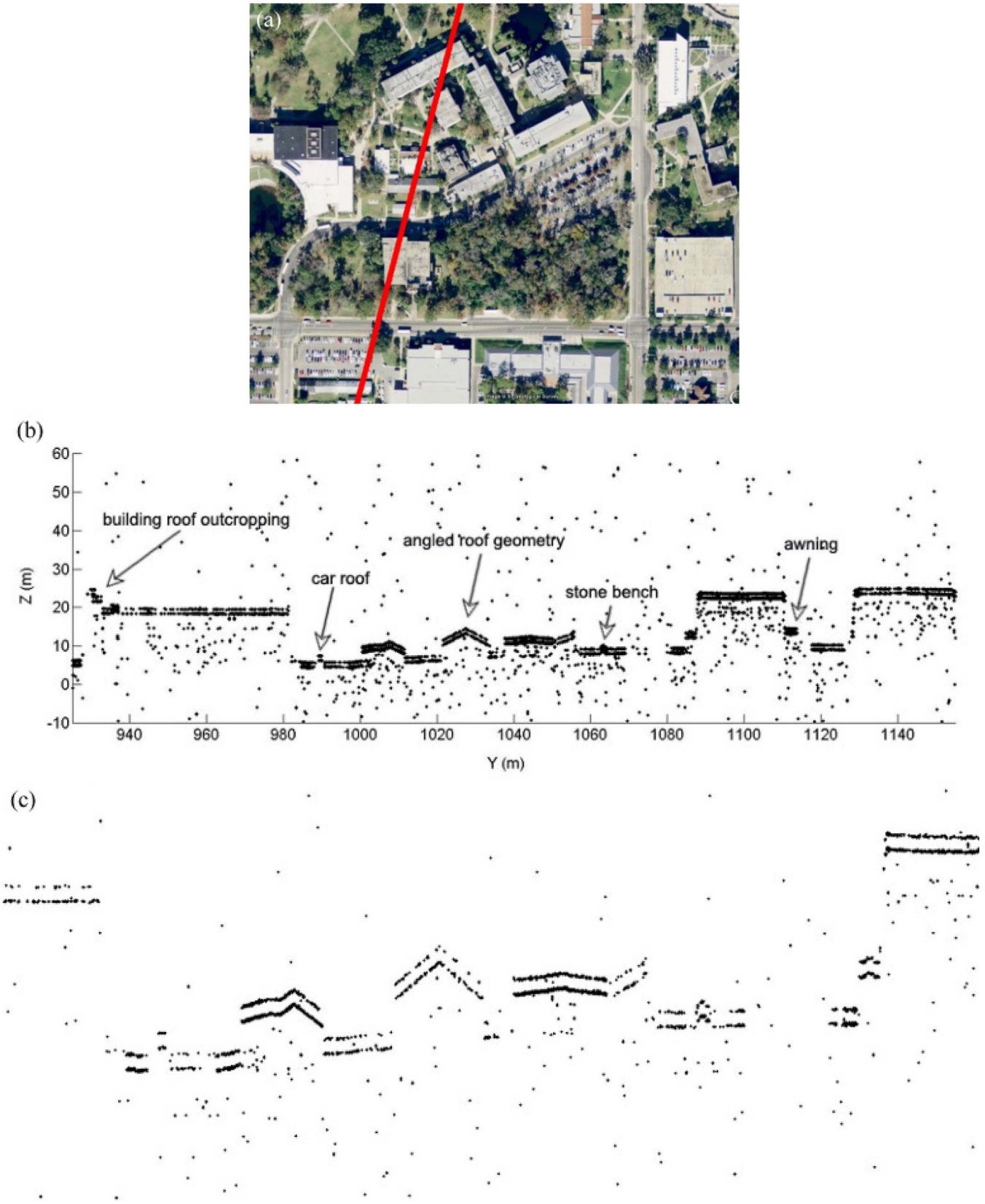


Fig. 4. Flight testing in Gainesville, FL, over the University of Florida campus. (a) Aerial photograph with a flight line. (b) Profile data from channels 20 and 23, 2300 V, all returns, with the unfiltered data showing vertical resolution capability in structure identification. (c) Zoom-in on data errors.

become much more evident; the number of above-ground points slightly increases as expected, but the large number of below-ground returns is now a stark contrast. In addition, note that the data errors are more pronounced below single scattering surfaces, i.e., bare earth and building roofs. This effect persists even through overlapping first-return data.

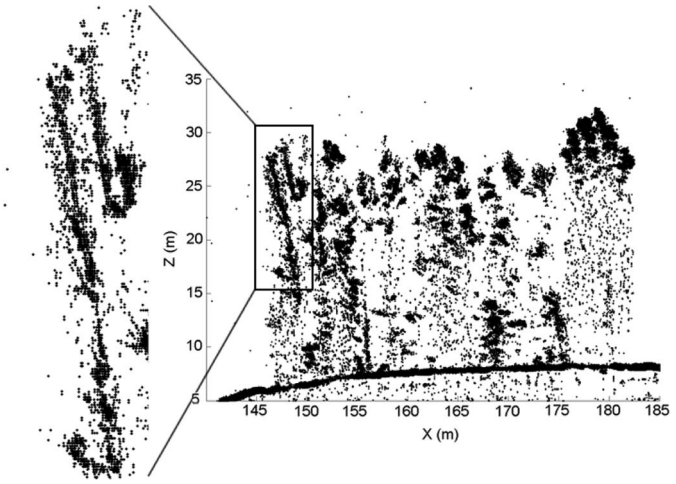


Fig. 5. Flight testing in Mine Run, VA, over a forested region. Small leaf structure elements are definable along with trunk and ground information.

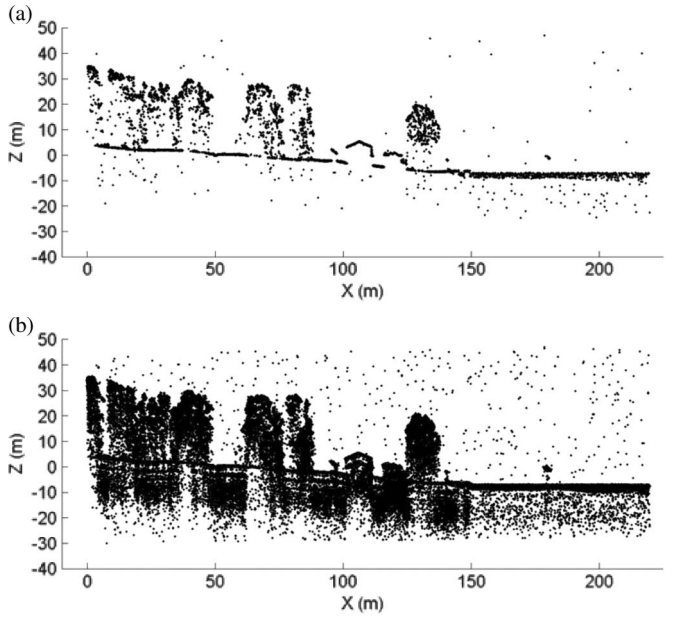


Fig. 6. Flight testing in Mine Run, VA, over a forested region. (a) Channel 23, first returns plotted. (b) Channels 17–32, all returns plotted.

### C. Local Density Calculations

Although it appears clear in Fig. 6 that errors below strongly reflective surfaces are significant, further quantification may aid in pattern identification and processing efforts. Estimates for local density in selected regions within the point cloud were computed. A segment of flat-ground data was manually windowed to encompass expected signal returns. Ghost responses should exhibit well-defined correlation to this window; the temporal offsets of the expected highest correlation are shown in Fig. 7 as "afterpulse 1/2." By then vertically sliding the true signal window as shown in Fig. 8 and expressing the correlation coefficient as a ratio of true signal to the measured effect, the plots in Fig. 9 were generated. In Fig. 9(a), the amount of correlation exponentially decreases, starting at zero distance (correlation % of 1.0) down to the noise floor, which is below a correlation % of 0.1. The ghosting correlation is not distinguishable in this plot. This result indicates that the spatial distributions of the ghost effects are significantly less dense than the true signal; therefore, a logarithmic $y$-scale is included to observe the output characteristics near the noise floor. If we fit a Gaussian profile to the data and measure the peaks, the largest correlation occurs at 12.67 and 24.00 ns, with peaks of 0.0085 and 0.0053, respectively.

### D. Causes of Image Ghosting

We can posit several explanations for the ghost image effect. First, gas impurities in the tube envelope could generate additional responses beyond the initial high-intensity return, which is commonly referred to as "afterpulsing" in nuclear particle physics experiments. Second, the cable that connects the PMT output to the high-speed data interface could have an impedance mismatch. A mismatch could cause undesirable reflections from the interface junctions to become significant at very large signal levels. Third, the silicon germanium high-speed gain block could be overdriven in cases of large signal output. This case would cause the amplifier to operate beyond the maximum recommended ratings, thereby inducing anomalous effects.

*1) PMT Afterpulsing:* Exploration into the chemical and physical nature of PMT afterpulsing effects [33]–[35] showed that diffusion of trace gases through the tube envelope contributed to an increase in the probability of pulse formation. In particular, diffused helium was found to be the main source of afterpulses in tubes that are more than two years old. In contrast, the contribution from this impurity in new tubes was often small [35]. An exponentially decaying low-level background signal has been shown to occur after the abrupt termination of a submicrosecond light pulse [36]. Positive ions that were produced during the ionization of residual gas in the PMT by PEs produce secondary electrons during their drift back onto the photocathode, which are then amplified [37], [38]. Other possible explanations for both short-term (submicrosecond) and long-term (microsecond to millisecond) responses are electron-induced luminescence of the dynodes or their support structures and microdischarges produced during high-gain operation [36].

Because the CATS uses a MCP-PMT that was manufactured in 2004 and has undergone significant use, it is possible that trace amounts of atmospheric gas diffused into the envelope over time may have risen to significant levels. However, because ghost images occur at highly consistent spacing, it is unlikely that PMT afterpulsing is the main source of the errors. Quantifying the amounts of impurities is beyond the scope of this paper, but potential contributions from afterpulsing should be mentioned due to the age of the tube.

*2) Impedance Matching:* The relationship between errors and dynamic range suggests that the cabling may be a factor. For radio frequency (30 kHz–300 GHz) circuitry, the impedance of the transmission line itself becomes significant. To maintain the maximum power transfer, the characteristic impedance of the cable $(Z_O)$ should be closely matched to the source $(Z_S)$ and load $(Z_L)$. If the total path length is greater than 10% of the signal wavelength, mismatch effects can have a greater impact. In the CATS system, 2-GHz-level signals mean that transmission lines that are longer than 4 cm must be well matched (assuming a velocity factor of 0.8).

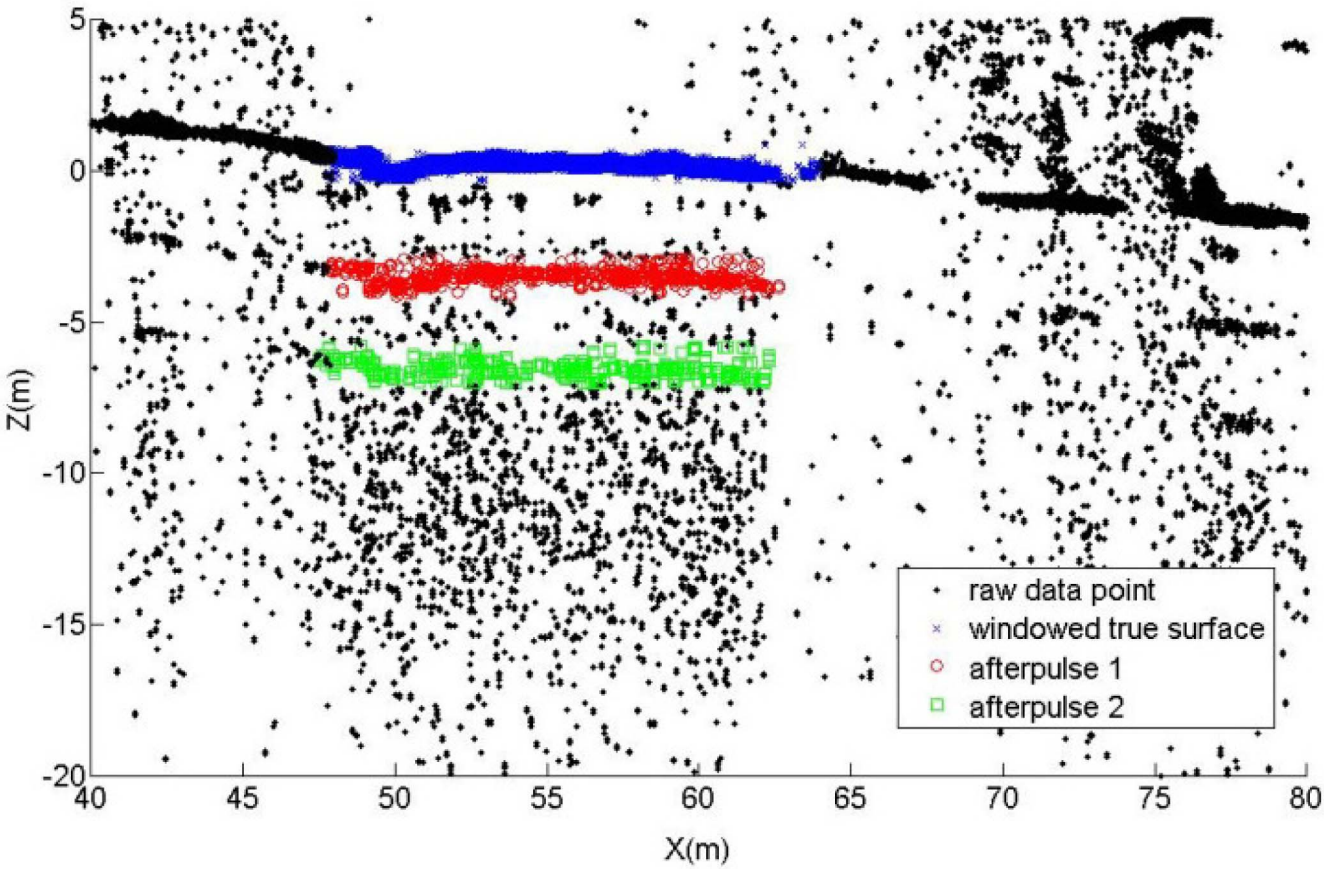


Fig. 7. Identifying afterpulsing effects in raw data.

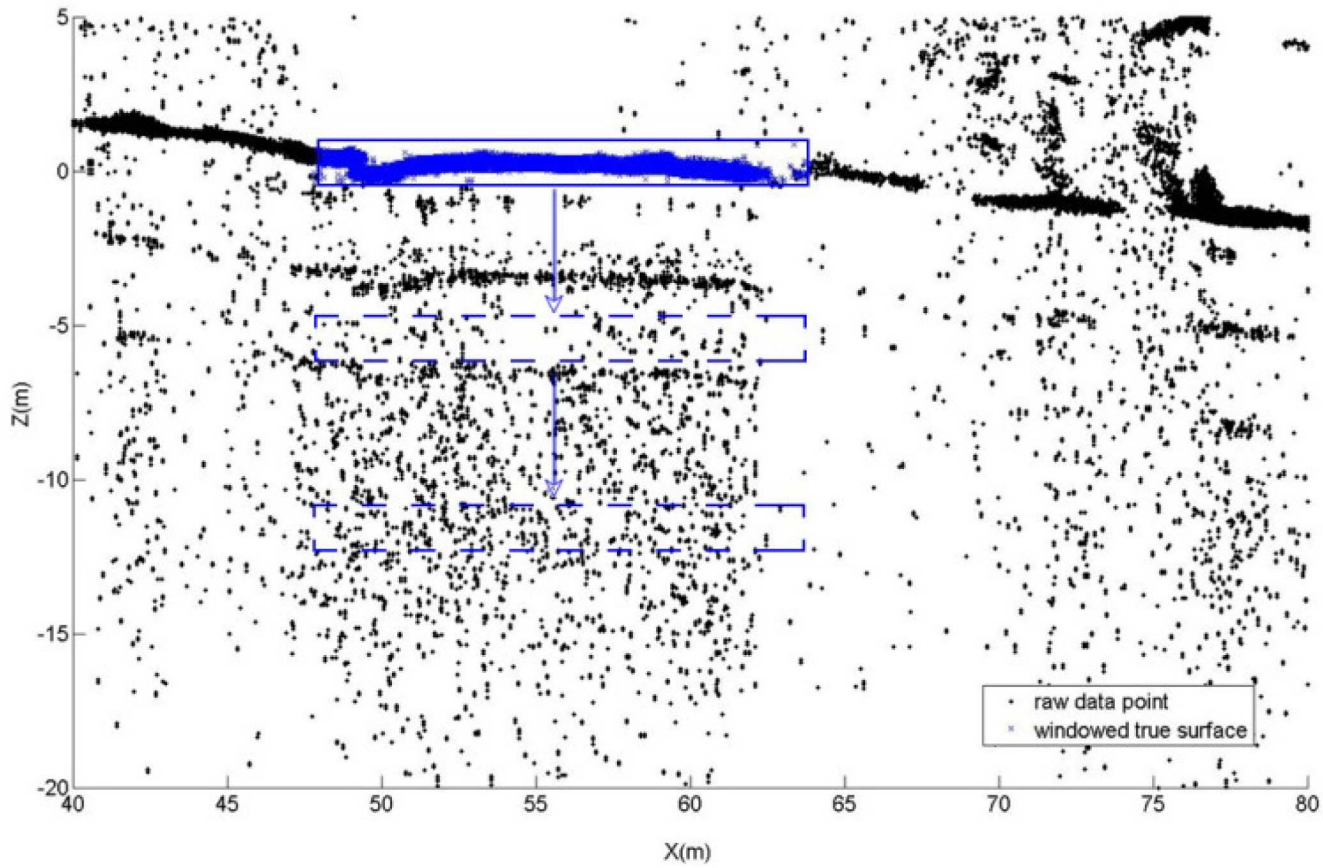


Fig. 8. Vertical sliding window to evaluate the magnitude of afterpulsing responses.

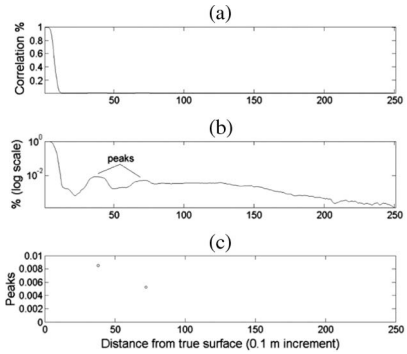


Fig. 9. Correlation of the windowed true signal to the afterpulsing signal in 0.1-m increments, starting from the true surface (correlation coefficient of 1.0). (a) Normal-scale $y$-axis. Peaks are indistinguishable. (b) Log-scale $y$-axis. Ghost peaks are visible. (c) Magnitude of peaks are both less than 1%.

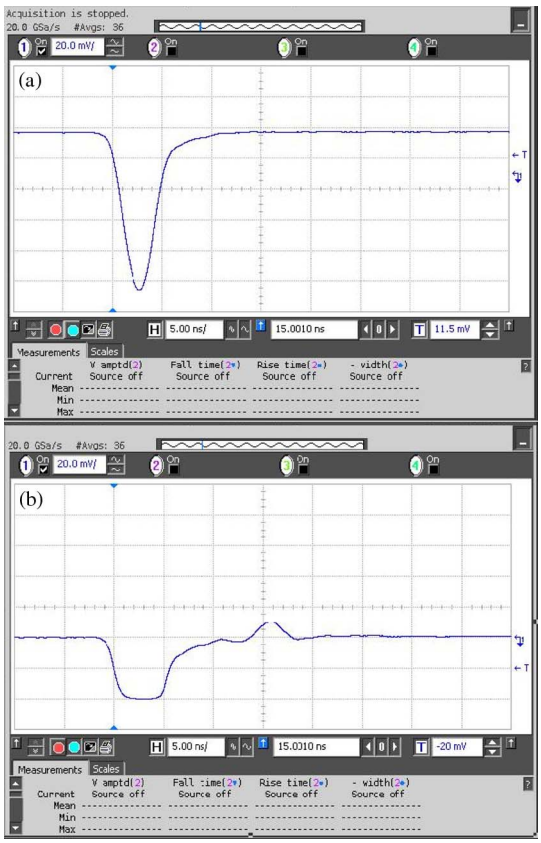


Fig. 10. (a) Large signal (110 mV) injected into the gain block. (b) Output of the gain block (courtesy of Fibertek Inc.).

After considering the layout of associated PCBs in the receiver design and estimating the total length between the PMT and data capture elements, the first reflection in both worst case scenarios is expected to be three orders of magnitude smaller than the true signal. The second reflection is six orders of magnitude smaller. Although potential reflections that result from worst case impedance mismatch may occur at the same temporal spacing as the ghost images, we conclude that the magnitudes should not be significant.

*3) Gain Block Overdrive:* Output signals are amplified by a 4000-MHz, 2.8-V SiGe gain block that was manufactured by Sirenza Microdevices (part number SGA-1263). The output of this device is directly fed into the threshold comparator for

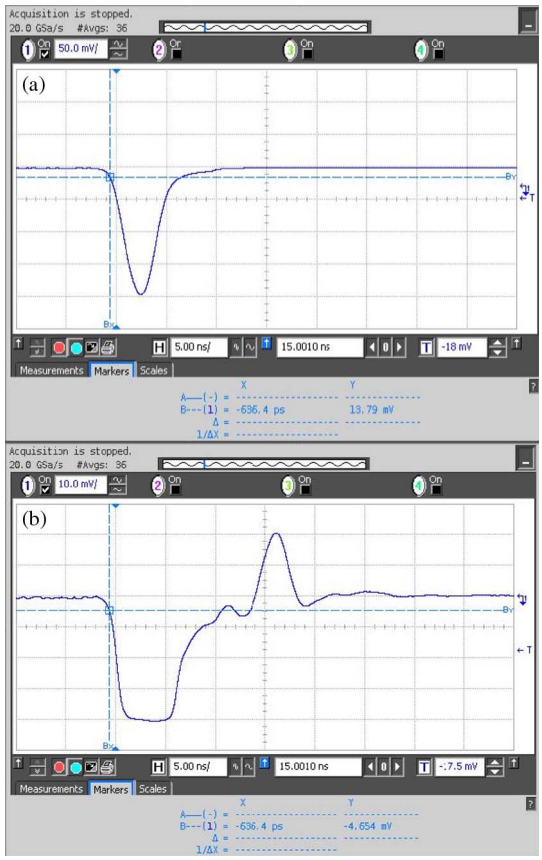


Fig. 11. (a) Larger signal (200 mV) injected into the gain block. (b) Output of the gain block (courtesy of Fibertek Inc.).

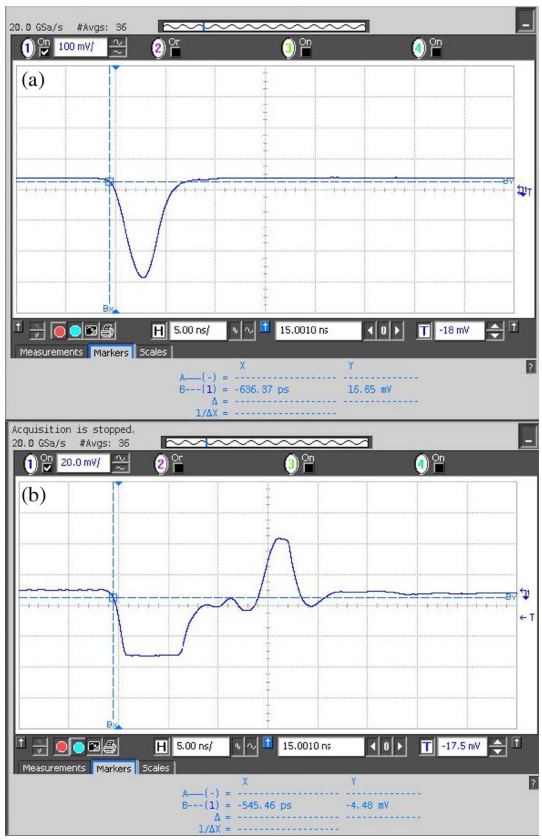


Fig. 12. (a) Largest signal (300 mV) injected into the gain block. (b) Output of the gain block (courtesy of Fibertek Inc.).

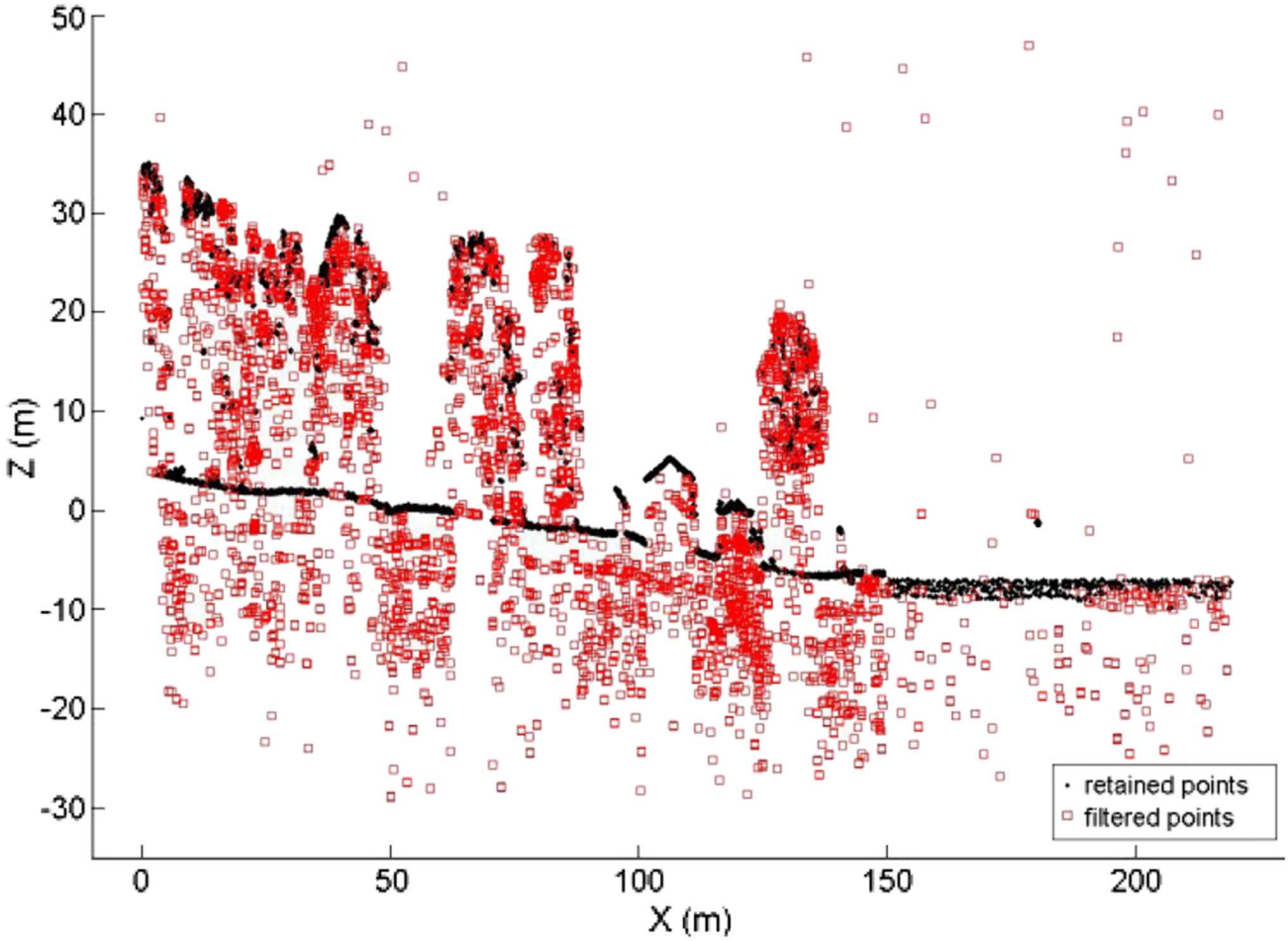


Fig. 13. Result of the first step of local density filter for a single channel of raw airborne profile data.

each channel. Because the system needs to operate on a single-photon sensitivity level, channel thresholds are set to a 4-mV trigger. According to the manufacturer's data sheet, the gain block has a maximum RF input power of $-12$ dBm or 63 $\mu$W, which equates to 56 mV into a 50-$\Omega$ load. An output current that is more than 1.1 mA will therefore begin to overdrive the gain block.

In Fig. 10(a), a large signal (110 mV) is injected into the gain block. This is approximately 25 times larger than a signal expected to barely produce a threshold crossing (4 mV). The resulting output is shown in Fig. 10(b). The desired response is the first large negative pulse. Deviations from the zero level in the waveform after the first negative pulse are anomalous effects that result from the large signal input. Here, we see small negative deformations before and after a positive peak. If we inject a larger signal, e.g., 200 mV [Fig. 11(a)], the output shown in Fig. 11(b) is produced. A line is drawn here to approximate the threshold crossing. The second crossing occurs at approximately 13 ns. If a still-larger signal, e.g., 300 mV [Fig. 12(a)], is injected into the block, we can identify threshold crossings in Fig. 12(b) at approximately 13 and 20 ns. The temporal spacings of these outputs are similar to spacings that were estimated from local density correlation within the point cloud. Because surface ghosting is exacerbated as the return intensity increases, it is likely that the gain block overdrive is the main culprit.

### *E. Data Filtering Based on Local Density Estimation*

We previously theorized that an LSNR LiDAR that operates with simple fixed threshold detection may be worth considering when coupled with short laser pulsewidth and dense point spacing. The extent to which this approach can be successful depends on the ability to locally separate coherent features from contaminating sources of noise, i.e., thermal, solar, and atmospheric effects. If point clouds that result from data that contain potentially corruptive data artifacts (such as the aforementioned ghosting) can be filtered to still retain pertinent feature structure, it is a testament to the instrument potential when the hardware is adjusted to eliminate error production. In the previous section, calculations showed that comparative spatial densities of ghost data errors are fairly small, i.e., peaks less than 1% of the true signal. We can thus perform point cloud filtering based on local points and expect not to lose a significant amount of signal information about strongly reflective, spatially coherent surfaces. We should apply this idea to corrupted LSNR ALB data and evaluate whether relative feature measurements are comparable to the ground truth. Generated algorithms should be near automatic, i.e., with the least possible manual input.

Fig. 13 shows filtering operations on a raw land/water data set. First, a decision boundary for the coastline ($\mathrm{x} = 150$ m) was estimated using a windowing approach similar to Fig. 8. Based on the number of points in a 3-D cube of space centered at each return, local density estimates were produced for

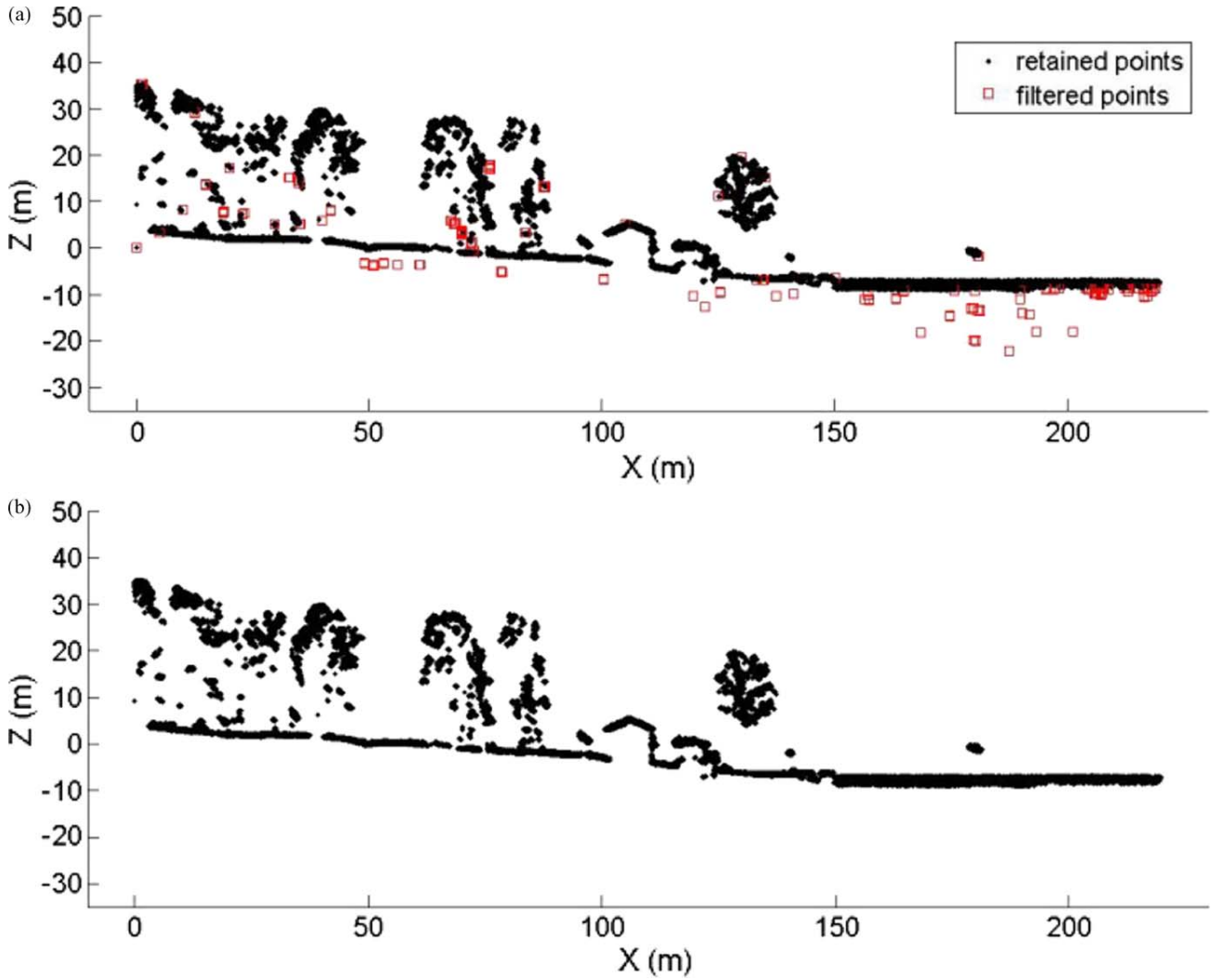


Fig. 14. Result of the second step of local density filter for raw airborne profile data. (a) Retained and filtered points. (b) Retained points only.

topographic data ($x < 150$ m) and bathymetric data ($x > 150$ m). The process is identical to the spatial correlation feature filter described in [32], which operates on the theory that noise events, although cumulatively occurring in a large quantity, sparsely occur in the context of local neighborhoods. One important assumption is that the probability of noise events with one or more local neighbors is less than 1.5%; Figs. 13 and 14 evaluate the merits of this assumption using sensor data.

Expected thresholds for noise points in each case, topographic and bathymetric, were calculated. Each return that exhibits a local density estimate below these thresholds were identified (indicated by squares in Fig. 13). The data were then filtered to retain all other points. Fig. 14 shows a second filtering step using a similar local density estimation process. The secondary step helps eliminate the few remaining artifacts, and the final processed image is shown in Fig. 14(b). A dense clump of points 5 m above the water surface is visible at $x = 180$ m; this is the result of returns from an overhanging island tree near the flight line. Because the density of returns suggests that this noise is not atmospheric, the filter retains the associated points.

## V. Analysis of Results

### A. Freshwater Bottom Mapping

The major goal of flight testing for the CATS instrument was to evaluate LSNR water penetration capabilities. The automated filtering process described in Section IV was used to produce a freshwater data set. A zoom-in view of filtered data from a shallow-lake area (southwest portion of the Lake of the Woods) in Mine Run is shown in Fig. 15(b). The path of the aircraft near the shoreline is indicated in Fig. 15(a). Data were collected during late-evening/night conditions under very calm surface conditions. The water in this area contained low amounts of colored dissolved organic material. The Secchi depth was measured by lowering a black-and-white painted disk into near-shore water until the pattern was no longer visible, which is an inexpensive straightforward procedure. Note, however, that Secchi readings are not necessarily the most accurate for absolute turbidity measurement; readings can vary, depending on ambient light conditions, human eyesight, and water surface glare.

To minimize errors, measurements were taken off the shady side of a boat at approximately 2 P.M. by a single observer. The

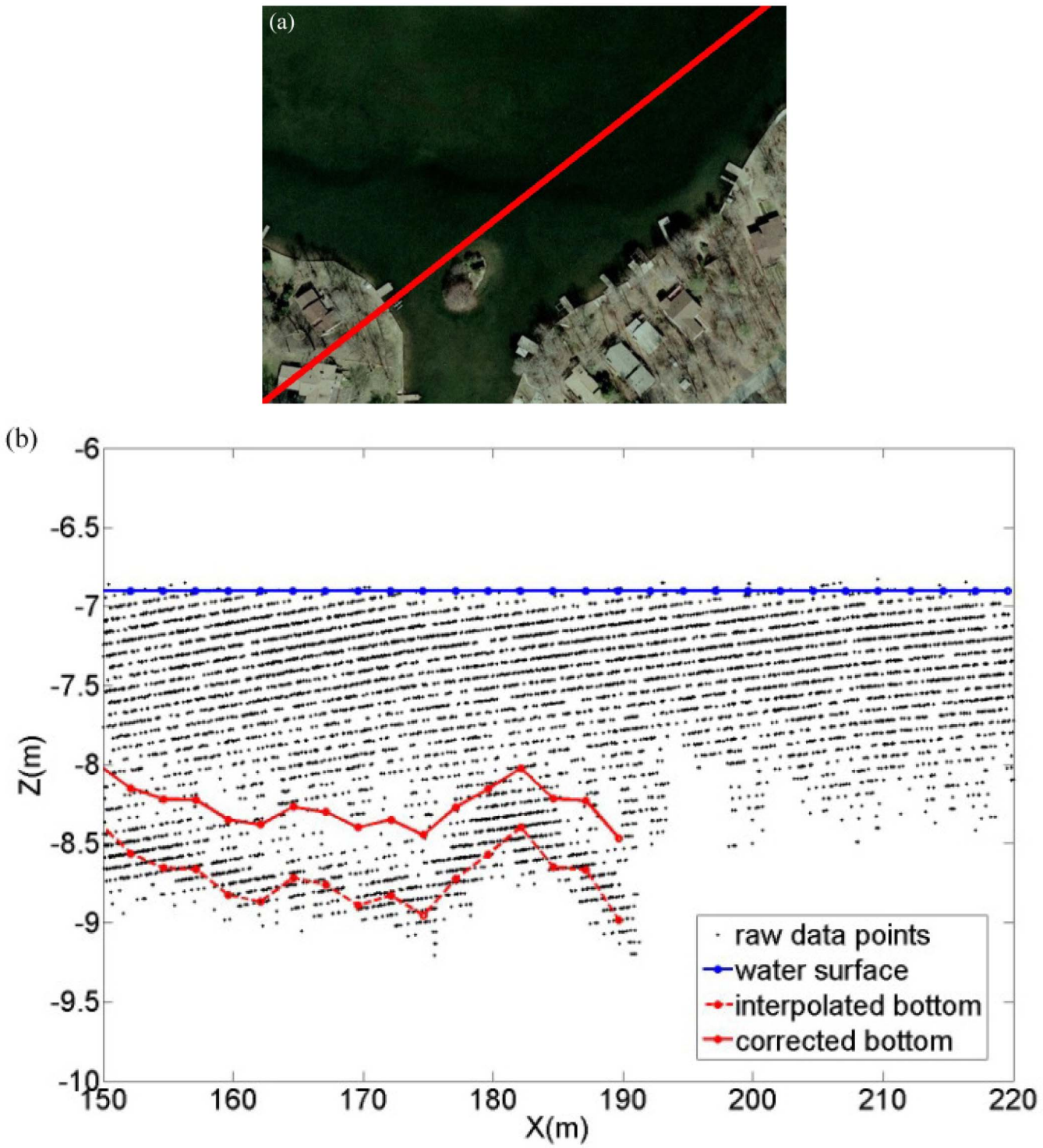


Fig. 15. Flight testing in Mine Run, VA, over the Lake of the Woods, southwest. (a) Aerial photograph near boat docks and shallow launch region with a flight line. (b) Off-nadir profile, channels 17–32, 2500 V, all returns, with the processed data depicting freshwater penetration out to 1.65 m.

purpose of these measurements was to provide a relative comparison of water turbidity for different areas of the lake (and, thus, for different bottom compositions). In the southwest area of the lake, the bottom was a mixture of dark sand and decaying organic material; the bottom reflectivity was very low. The Secchi depth here was 2 m. Sixteen channels of data were collected at 2500 V or maximum PMT amplification. Manual measurements of water depths in this area at 10-m intervals were also performed using a measuring tape with an attached weight.

TABLE II
COMPARISON OF LIDAR DEPTH ESTIMATES AND MEASUREMENTS

| X (m) | 150 | 160 | 170 | 180 | 190 | 200 |
|---|---|---|---|---|---|---|
| LiDAR Depth Estimate (m) | 1.12 | 1.45 | 1.49 | 1.24 | 1.65 | NA |
| Depth Measurement (m) | 1.27 | 1.52 | 1.65 | 1.52 | 2.03 | 2.44 |
| Difference (m) | 0.15 | 0.07 | 0.16 | 0.28 | 0.38 | NA |

Point cloud values were interpolated to estimate the lake bottom surface, as shown in Fig. 15(b), dashed line. The interpolated bottom was then corrected for the index of refraction

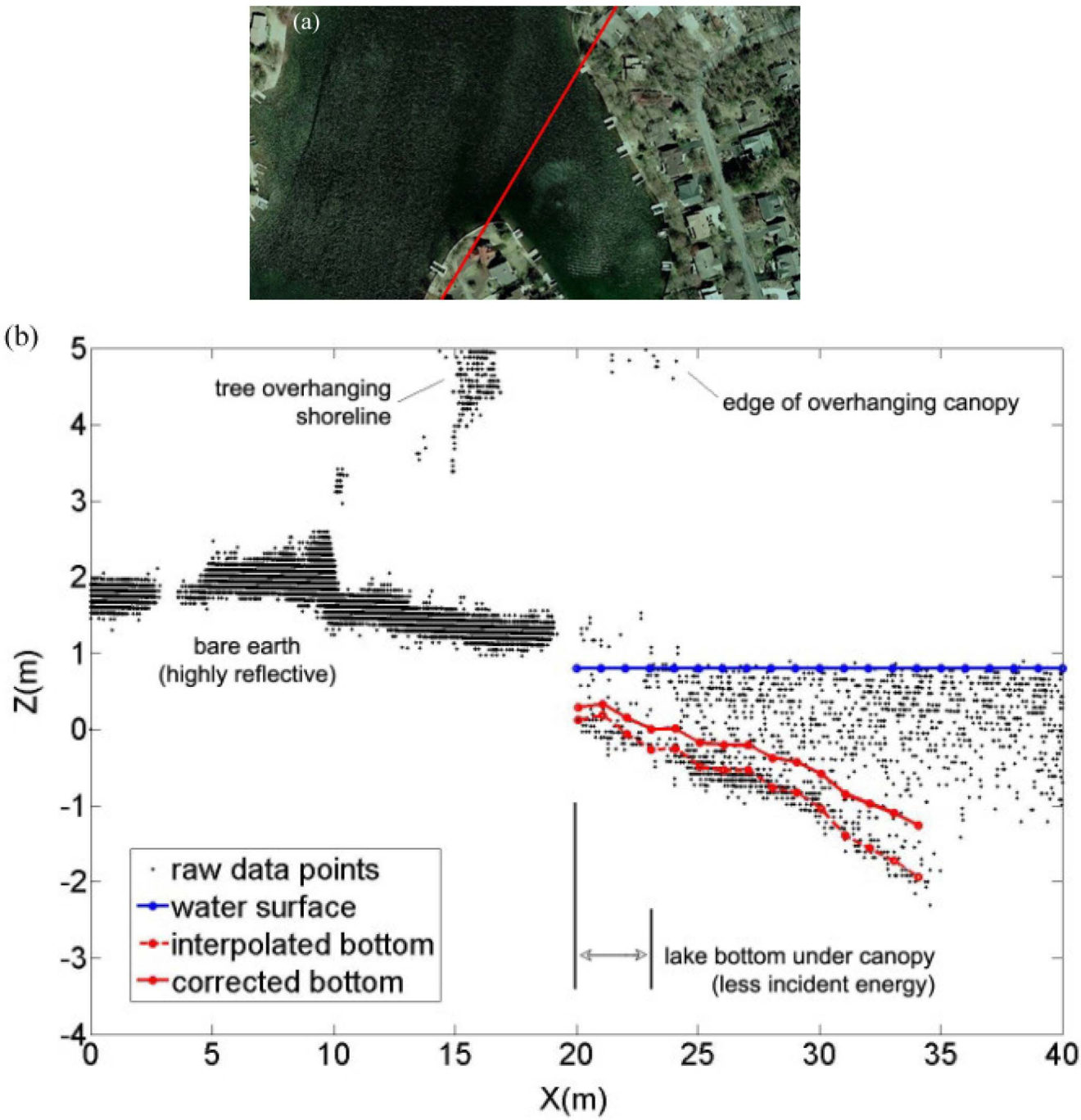


Fig. 16. Flight testing in Mine Run, VA, over the Lake of the Woods, northeast. (a) Aerial photograph near the lake shoreline with a flight line. (b) Off-nadir profile, channels 17–32, 2500 V, all returns, with the processed data depicting freshwater penetration out to 2.10 m.

of water (1.33), as shown in Fig. 15, solid line. Here, we see a consistent response from the water surface, as shown in Fig. 15, flat line, and an exponential decay of water column returns progressing to further depth. The lake bottom produces a strong signal at 1–1.3 m depths near the shoreline at $x = 150$ m. Water depths at 10-m horizontal intervals were extracted from the LiDAR data in this region by differencing the interpolated water surface and corrected lake bottom function. Lake bottom returns become negligible at a water depth of approximately 1.65 m. There was a large amount of sediment buildup from organic/inorganic particulate near a small island located at $x = 180$ m. This case could lead to a shortening of the estimated depth near the island. Table II compares LiDAR depth estimates to measured values. The average difference between estimates and measurements is 21 cm. The central 16 channels (17% of the total footprint area) were sufficient in the profile mode to reconstruct the bottom. At a depth of 0.5–1.5 m, on the average, 38 returns per meter were registered from the lake bottom. For an 8-kHz laser pulse rate and 60-m/s flight speed, this result corresponds to an average of 1.77% of the outgoing shots that register returns from the lake bottom.

Fig. 16 shows a location to the northeast where the bottom was composed of a mix of lighter sand and organic material. The Secchi depth here was also 2 m, which means that the water

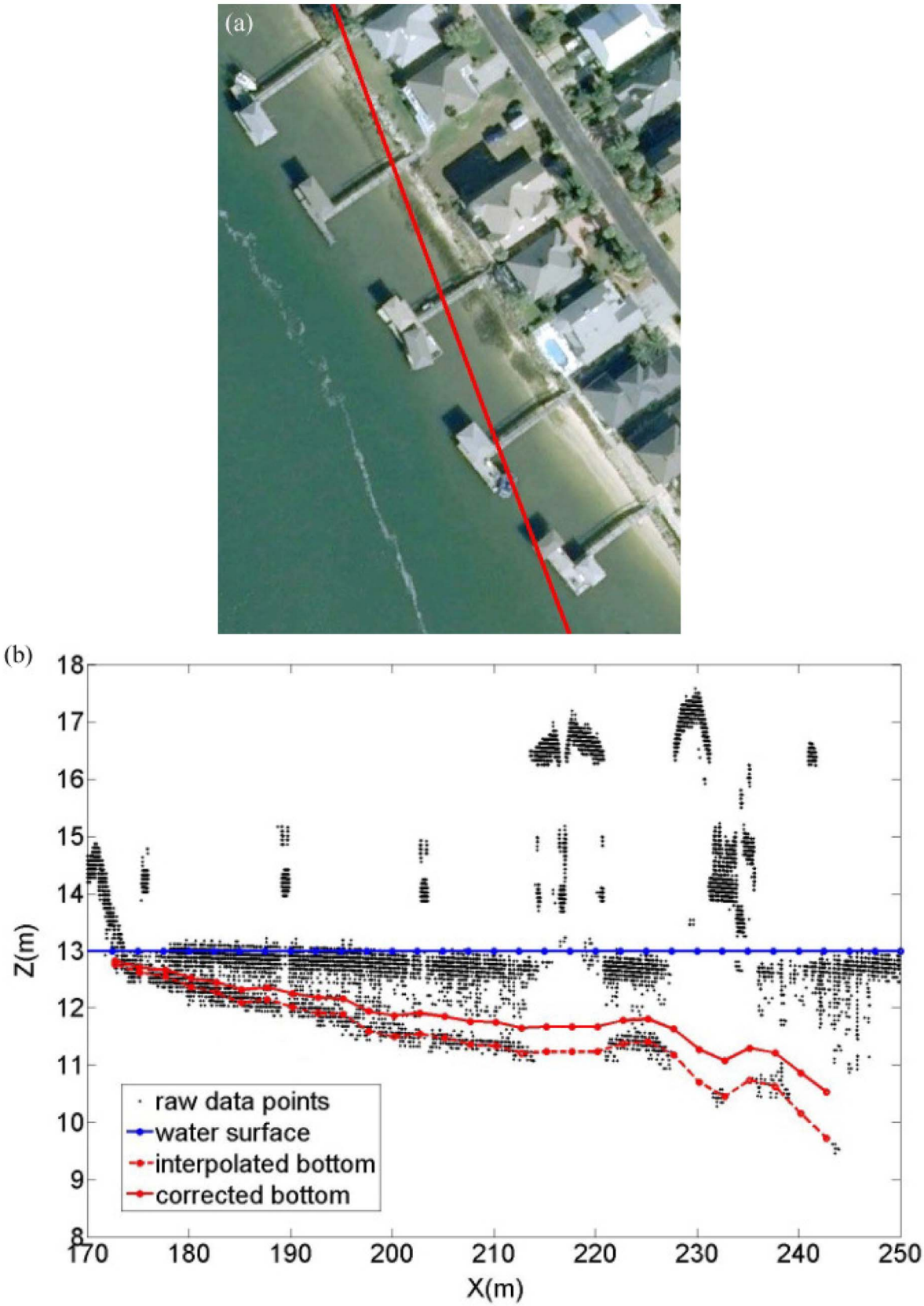


Fig. 17. Flight testing in St. Augustine, FL, over docks on the Intracoastal Waterway. A slight roll of the aircraft is most likely present, causing the interrogated profile to be displaced approximately 1 m to the left of the red flight line in the aerial photo. (a) Aerial photograph near boat docks and shallow launch region with a flight line. (b) Off-nadir profile, single channel (18), 2500 V, all returns, with the processed data depicting saltwater penetration out to 2.5 m. Note the compression of the $x$-axis (necessary to depict the entire range of bottom sensing).

TABLE III
COMPARISON OF LIDAR PLATFORM DISTANCE ESTIMATES AND MEASUREMENTS

| X (m) | 175 | 189 | 203 | 214 | 236 |
|---|---|---|---|---|---|
| LiDAR Platform Estimate (m) | 1.68 | 2.13 | 2.37 | 2.53 | 2.90 |
| Platform Measurement (m) | 1.82 | 2.20 | 2.59 | 2.74 | 3.12 |
| Difference (m) | 0.14 | 0.07 | 0.22 | 0.21 | 0.22 |

turbidities for the southwest and northeast portions of the lake were consistent. An off-nadir profile for 16 channels at 2500 V depicts recovery of the lake bottom out to a 2.10-m depth. The increase in reflectivity is the expected cause of increased returns from the lake bottom at a greater depth. Fewer bottom returns near the shoreline were received as a result of overhanging tree branches, but multiple returns still provided information about submerged surfaces. At a depth of 1–2 m, on the average, 74 returns per meter were registered from the lake bottom. This result corresponds to an average of 3.49% of the outgoing shots that register returns from the lake bottom.

### B. Saltwater Bottom Mapping

Further flight testing was conducted over the Intracoastal Waterway, St. Augustine, FL, under full daylight conditions. Fig. 17 shows point cloud data starting from the shoreline and out to a boat dock 60 m away. The water surface and bottom profile between boat docks and a shallow boat launch region are depicted. Note the compression of the $x$-axis in the plotted data (necessary to depict the entire range of bottom sensing). Dense clusters of points that are 1–2 m above the water surface are a result of narrow wooden walkways ($\mathrm{x} = 175, 189, 203$ m) that lead out to the boathouses. The sand bottom was reflective enough in this case for a single channel to provide bottom reconstruction out to a depth of 2.50 m. Hand measurements of wood platform heights above the water surface were performed at five locations (Table III, third row). LiDAR estimates of platform heights were calculated by getting the difference of the first above-water return that is associated with the wood surface and the interpolated bottom at the five indicated locations (Table III, second row). The comparison of measurements to estimates yields an average error of 17 cm.

Fig. 18 shows information from three channels over a sand bar in the St. Augustine Intracoastal Waterway. Bottom features out to a depth of 1.5 m are recovered here in high detail; submerged pockets and dunes are identifiable, because currents have affected the sand geometry. An aerial photograph of the east coast of Florida near St. Augustine with the aircraft path is shown in Fig. 19. The associated point data from three channels extend from the beach out to open water and are colored according to elevation. Of particular interest in this image are the gradually increasing sea floor slope in the surf zone near the beach–water interface and the sand bar located 40 m from the shore.

A single channel of information (1% of the total footprint area) was used in the profile mode to reconstruct a saltwater intracoastal floor (estimated to be highly reflective) in water of high clarity out to 2.5 m. At a depth of 1–2 m, on the average, 45 returns per meter were registered from the submerged floor. This result corresponds to an average of 33.98% of the outgoing shots that register returns from the floor; these are assumed to be near-ideal turbidity conditions. Three channels of information (3% of the total footprint area) were used in the profile mode to reconstruct the sea floor (estimated to be highly reflective) in the surf zone near a beach in water of optimum clarity out to 2 m. At a depth of 1–2 m, on the average, 56 returns per meter were registered from the sea floor. This result corresponds to an average of 13.98% of the outgoing shots that register returns from the floor.

## VI. CONCLUSION

This paper has discussed results from airborne tests of a prototype LSNR ALB instrument. Analysis of topographic data identified significant issues related to "ghost surfaces," and gain block overdrive was identified as the most likely cause of the ranging errors. A data-processing methodology based on local density estimation was proposed to correct corrupted data. Analysis of corrected airborne profile data from the CATS over a freshwater lake in Mine Run, VA, and saltwater areas near the eastern coast in St. Augustine, FL, has yielded submerged surface reconstruction for practical water turbidities/surface reflectances down to 2.5-m depths. We have shown continuous mapping of the near-depth shore with limited discontinuity at the land–water interface. Depth calculations from CATS data estimate average range errors of 17 and 21 cm in freshwater/saltwater. This result was expected, because there were no attitude corrections for profile data.

### A. Suggestions for Future Improvements

For mixed mapping, it is difficult to automatically process topographic and bathymetric data simultaneously with the current CATS detector structure. The dynamic range between building roofs/bare earth and water surface/column/bottom is very large. Areas such as marsh wetlands can cause trouble for feature extraction algorithms that manipulate local densities. Range bin "stacking" caused by highly reflective surfaces can also override multiple events from distributed laser backscatter through closely spaced vertical elements. One successful technique for combating this problem is to use several detectors at varying brightness sensitivity [5], [14], [24] to characterize returns based on saturation levels.

In the Optech SHOALS system, the dynamic range problem is handled by using one high-gain PMT and one low-gain APD. The high-gain channel is gated on only after the pulse has passed through the air–water interface [24]. It may be possible to implement a similar "sensing" stage in the CATS to modify signal amplification on a dynamic level. For example, the high voltage is already stepped on a per-shot basis to reduce the power consumption and extend the PMT life. If a separate photodetector was placed in front of the primary MCP-PMT (whether physically or by temporal delay sequencing) such that it were possible to determine the intensity of the backscattered radiation before stepping up the tube high voltage, the level to which the voltage was stepped could dynamically be altered. It would then be possible to obtain different amplification for topographic returns as opposed to sea bottom returns with fairly minimal modification to the current system structure.

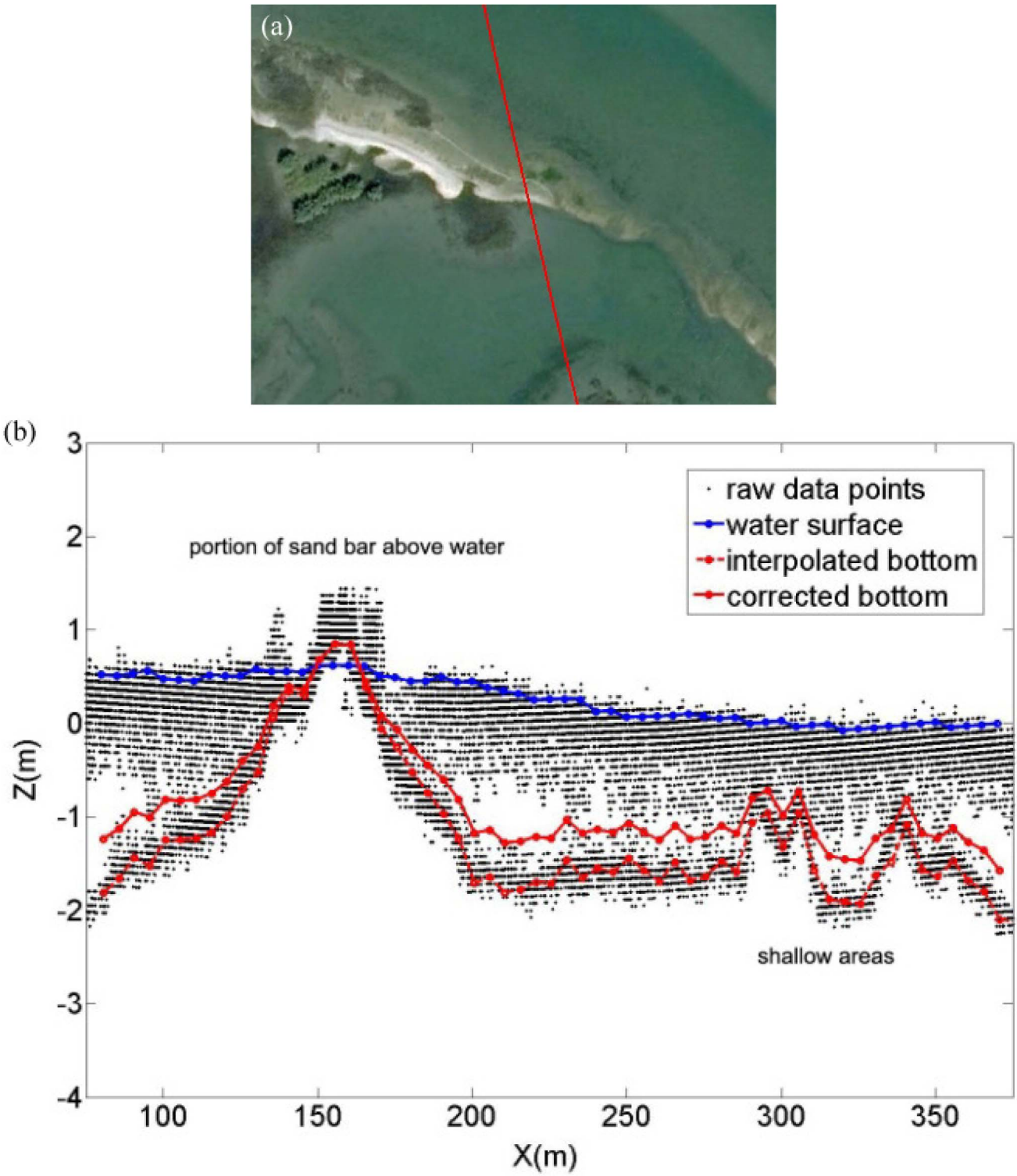


Fig. 18. Flight testing in St. Augustine, FL, over a sandbar on the Intracoastal Waterway. (a) Aerial photograph over a sand bar with a flight line. (b) Off-nadir profile, channels 21–23, 2500 V, all returns. Point cloud depicts sand bottom out to 1.5 m.

Operating in a multiphoton state has been shown to provide 70× less atmospheric noise [18] and still remains capable of ranging to buildings, tree trunks, and ground surfaces. A sensing stage could also improve the maximum water penetration depth. Although the MCP-PMT already operates at its maximum amplification, if the possibility of full amplification during periods of high-intensity laser backscatter (which can damage the detector) could be negated, it would be possible to fly lower than 500 m and lose less power in the atmosphere. The 10 × 10 array output is eye safe down to 100-m altitudes; therefore, the only restricting factor even for populated areas is the Federal Aviation Administration (FAA) regulations. Flying

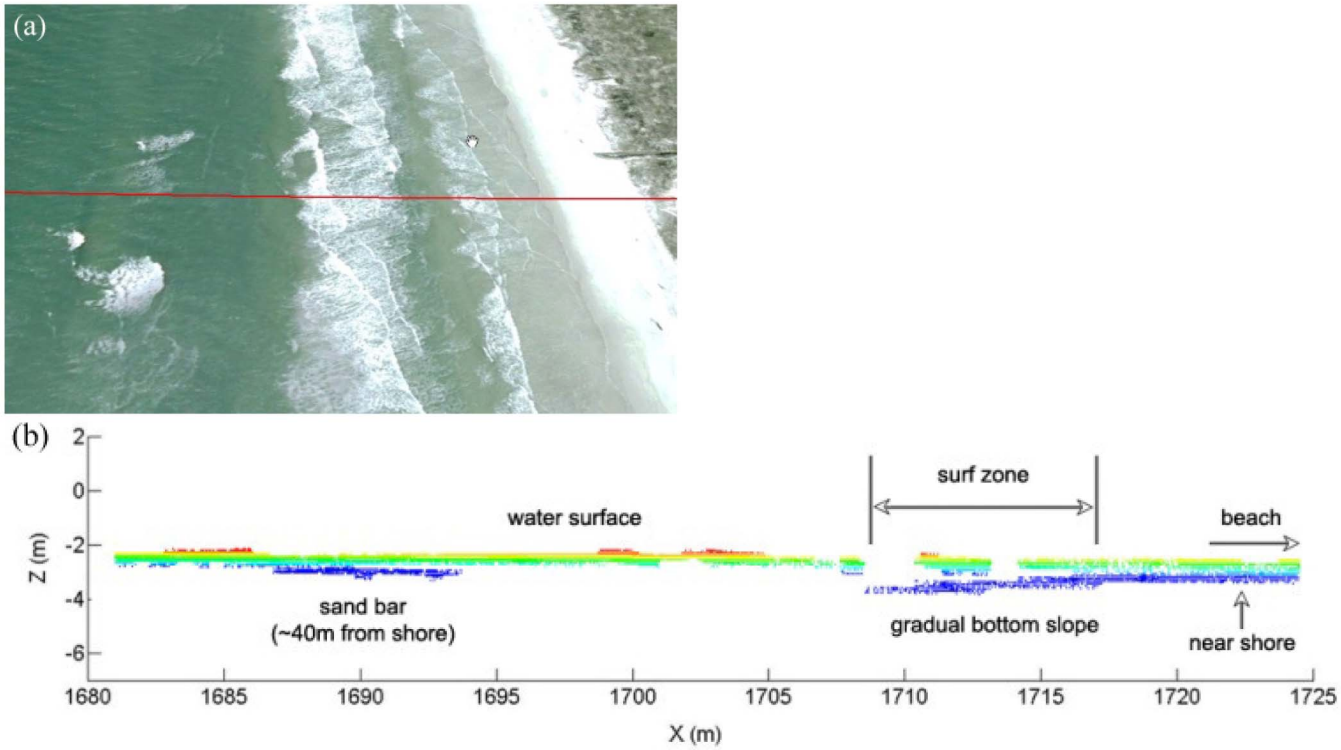


Fig. 19. Flight testing in St. Augustine, FL, over the eastern coast. (a) Aerial photograph of flight path relative to the beach. (b) Off-nadir profile, 2500 V, channels 21–23, all returns, with the processed data related to the beach–water interface region.

lower would also decrease the ground spacing between subpixel locations in the CATS footprint, creating improved spatial density and potentially reducing pitch and roll errors. One disadvantage of this approach is a narrower swath, which increases the flight time necessary to cover the same amount of area.

## REFERENCES

[1] K. Francis, P. LaRocque, L. Gee, and M. Paton, "Hydrographic LiDAR processing moves into the next dimension," in *Proc. U.S. Hydro*, 2003, pp. 1–18.

[2] H. H. Kim, P. O. Cervenka, and C. B. Lankford, "Development of an airborne laser bathymeter," NASA, Washington, DC, NASA Tech. Note TND-8079, Oct. 1975.

[3] W. J. Lillycrop, R. W. Pope, and J. M. Wozencraft, "Airborne LiDAR hydrography: Vision for tomorrow," *Sea Technol.*, vol. 43, no. 6, pp. 27–34, 2002.

[4] C. W. Wright, F. E. Hoge, R. N. Swift, J. K. Yungel, and C. R. Schirtzinger, "Next-generation NASA airborne oceanographic LiDAR system," *Appl. Opt.*, vol. 40, no. 3, pp. 336–342, Jan. 2001.

[5] C. W. Wright and J. C. Brock, "EAARL: A LIDAR for mapping coral reefs and other environments," in *Proc. 7th Int. Conf. Remote Sens. Mar. Coastal Environ.*, Miami, FL, 2002, Nat. Oceanic Atmos. Admin.

[6] P. E. LaRocque and E. Yang, "Enhancements to the new SHOALS 3000 system," in *Proc. Int. LiDAR Mapping Forum*, Denver, CO, Mar. 3–5, 2010, pp. 1–11.

[7] T. Cossio, K. C. Slatton, W. Carter, K. Shrestha, and D. Harding, "Predicting topographic and bathymetric measurement performance for low-SNR airborne LiDAR," *IEEE Trans. Geosci. Remote Sens.*, vol. 47, pt. 2, no. 7, pp. 2298–2315, Jul. 2009.

[8] J. Degnan, "Photon-counting multikilohertz microlaser altimeters for airborne and spaceborne topographic measurements," *J. Geodyn.*, vol. 34, no. 3/4, pp. 503–549, Oct./Nov. 2002.

[9] G. C. Guenther, P. E. LaRocque, and J. W. Lillycrop, "Multiple surface channels in SHOALS airborne LiDAR," in *Proc. SPIE*, 1994, vol. 2258, pp. 422–430.

[10] J. M. Wozencraft, "Complete coastal mapping with airborne LiDAR," in *Proc. MTS/IEEE Oceans*, 2002, vol. 2, pp. 1194–1198.

[11] S. Pe'eri and W. Philpot, "Increasing the existence of very shallow water LiDAR measurements using the red-channel waveforms," *IEEE Trans. Geosci. Remote Sens.*, vol. 45, no. 5, pp. 1217–1223, May 2007.

[12] A. Collin, P. Archambault, and B. Long, "Mapping the shallow-water seabed habitat with the SHOALS," *IEEE Trans. Geosci. Remote Sens.*, vol. 46, no. 10, pp. 2947–2955, Oct. 2008.

[13] G. C. Guenther, "Airborne laser hydrography: System design and performance factors," NOS, NOAA, Rockville, MD, A 639 884, Mar. 1985, NOAA Prof. Paper Ser.

[14] J. C. Brock, C. W. Wright, T. D. Clayton, and A. Nayegandhi, "LiDAR optical rugosity of coral reefs in Biscayne National Park, FL," *Coral Reefs*, vol. 23, no. 1, pp. 48–59, Apr. 2004.

[15] J. J. Degnan, "Unified approach to photon-counting microlaser rangers, transponders, and altimeters," *Surv. Geophys.*, vol. 22, no. 5/6, pp. 431–447, Sep. 2001.

[16] W. C. Priedhorsky, R. C. Smith, and C. Ho, "Laser ranging and mapping with a photon-counting detector," *Appl. Opt.*, vol. 35, no. 3, pp. 441–452, Jan. 1996.

[17] P. Villoresi, T. Jennewein, F. Tamburini, M. Aspelmeyer, C. Bonato, R. Ursin, C. Pernechele, V. Luceri, G. Bianco, A. Zeilinger, and C. Barbieri, "Experimental verification of a quantum channel between space and earth," *New J. Phys.*, vol. 10, p. 033 038, 2008.

[18] R. Gutierrez, A. Neuenschwander, and M. M. Crawford, "Development of laser waveform digitization for airborne LiDAR topographic mapping instrumentation," in *Proc. IGARSS*, Jul. 25–29, 2005, pp. 1154–1157.

[19] K. Y. Shrestha, K. C. Slatton, W. E. Carter, and T. K. Cossio, "Performance metrics for single-photon laser ranging," *IEEE Geosci. Remote Sens. Lett.*, vol. 7, no. 2, pp. 338–342, Apr. 2010.

[20] G. C. Guenther, A. G. Cunningham, P. E. LaRocque, and D. J. Reid, "Meeting the accuracy challenge in airborne LiDAR bathymetry," in *Proc. EARSeL-SIG Workshop on LIDAR*, 2000, pp. 1–27.

[21] C. Hug, A. Ullrich, and A. Grimm, "Litemapper-5600—A waveform-digitizing LiDAR terrain and vegetation mapping system," *Int. Arch. Photogramm., Remote Sens. Spatial Inf. Sci.*, vol. 36, pt. 8/W2, pp. 24–29, 2005.

[22] C. Mobley, *Light and Water: Radiative Transfer in Natural Waters*. New York: Academic, 1994.

[23] C. Mallet, F. Lafarge, M. Roux, U. Soergel, F. Bretar, and C. Heipke, "A marked point process for modeling LiDAR waveforms," *IEEE Trans. Image Process.*, vol. 19, no. 12, pp. 3204–3221, Dec. 2010.
[24] G. C. Guenther, "Airborne LiDAR bathymetry," in *Digital Elevation Model Technologies and Applications: The DEM User's Manual*, 2nd ed, D. Maune, Ed. Bethesda, MD: Amer. Soc. Photogramm. Remote Sens., 2007, ch. 8, pp. 253–320.
[25] V. I. Feygels, C. W. Wright, Y. I. Kopilevich, and A. I. Surkov, "Narrow-field-of-view bathymetrical LiDAR: Theory and field test," in *Proc. SPIE: Ocean Remote Sens. Imag. II*, 2003, vol. 5155, pp. 1–11.
[26] K. Albright, R. C. Smith, C. Ho, S. K. Wilson, J. Bradley, A. Bird, D. E. Casperson, M. Hindman, R. Whitaker, J. Theiler, R. Scarlett, and W. C. Priedhorsky, "RULLI: A photon-counting imager," in *Proc. IASI, Symp. Detection Anal. Sub-Surf. Objects Phenom.*, Monterey, CA, 1998, pp. 1–9.
[27] P. Cho, H. Anderson, R. Hatch, and P. Ramaswami, "Real-time 3-D ladar imaging," *Lincoln Lab. J.*, vol. 16, no. 1, pp. 147–164, 2006.
[28] P. B. Russel, T. J. Swissler, and M. P. McCormick, "Methodology for error analysis and simulation of LiDAR aerosol measurements," *Appl. Opt.*, vol. 18, no. 22, pp. 3783–3797, Nov. 1979.
[29] Z. Liu, W. Hunt, M. Vaughan, C. Hostetler, M. McGill, K. Powell, D. Winker, and Y. Hu, "Estimating random errors due to shot noise in backscatter LiDAR observations," *Appl. Opt.*, vol. 45, no. 18, pp. 4437–4447, Jun. 2006.
[30] B. M. Oliver, "Thermal and quantum noise," *Proc. IEEE*, vol. 53, no. 5, pp. 436–454, May 1965.
[31] H. R. Gordon, "Interpolation of airborne oceanic LiDAR: Effects of multiple scattering," *Appl. Opt.*, vol. 21, no. 16, pp. 2996–3001, Aug. 1982.
[32] T. K. Cossio, K. C. Slatton, W. E. Carter, K. Y. Shrestha, and D. Harding, "Predicting small target detection performance of low-SNR airborne LiDAR," *IEEE J. Sel. Topics Appl. Earth Obs. Remote Sens.*, vol. 3, no. 4, pp. 672–688, Dec. 2010.
[33] G. A. Morton, H. M. Smith, and R. Wasserman, "Afterpulses in photomultipliers," *IEEE Trans. Nucl. Sci.*, vol. NS-14, no. 1, pp. 443–448, Feb. 1967.
[34] R. Staubert, E. Bohm, K. Hein, K. Sauerland, and J. Trumper, "Possible effects of photomultiplier-afterpulses on scintillation counter measurements," *Nucl. Instrum. Methods*, vol. 84, no. 2, pp. 297–300, Apr. 1970.
[35] P. B. Coates, "The origins of afterpulses in photomultipliers," *J. Phys. D, App. Phys.*, vol. 6, no. 10, p. 1159, Jun. 1973.
[36] M. P. Bristow, "Suppression of afterpulsing in photomultipliers by gating the photocathode," *Appl. Opt.*, vol. 41, no. 24, p. 4957, Aug. 2002.
[37] Y. Kanaya and H. Akimoto, "Gating a channel photomultiplier with a fast high-voltage switch: Reduction of afterpulse rates in a laser-induced fluorescence instrument for measurement of atmospheric OH radical concentrations," *Appl. Opt.*, vol. 45, no. 6, pp. 1254–1259, Feb. 2006.
[38] N. Akchurin and H. Kim, "A study on ion-initiated photomultiplier afterpulses," *Nucl. Instrum. Methods Phys. Res.*, vol. 574, no. 1, pp. 121–126, Apr. 2007.

**Kristofer Y. Shrestha** (M'12) received the B.S. and Ph.D. degrees from the University of Florida (UF), Gainesville, in 2004 and 2010, respectively.

He is currently a Postdoctoral Fellow with the Department of Earth and Atmospheric Sciences, Georgia Institute of Technology, Atlanta. His research interests include low-SNR LiDAR, adaptive signal processing, automatic feature extraction, land surface modeling, numerical weather prediction, and probabilistic flood forecasting.

**William E. Carter** is currently a Research Professor with the Department of Civil and Environmental Engineering, University of Houston, Houston, TX, and a Co–Principal Investigator (PI) with the National Center for Airborne Laser Mapping (NCALM), National Science Foundation (NSF), Houston. At the time that the Coastal Area Tactical Mapping System (CATS) was developed, he was an Adjunct Professor with the Department of Civil and Coastal Engineering, University of Florida (UF), Gainesville, where he taught courses in geodesy and conducted research on advanced geodetic techniques, including airborne and ground-based laser scanning. His experience with laser ranging dates back to 1969 when, as a graduate student, he was a Member of a team that developed a lunar laser ranging observatory to make range measurements from the Earth to the Moon using retroreflector arrays placed on the Moon by National Aeronautics and Space Administration (NASA) Apollo astronauts and USSR unmanned lunar rovers. He is the author of two books and a coauthor or the author of more than 100 technical papers and articles.

**K. Clint Slatton** (S'95–M'02–SM'07) received the B.S. and M.S. degrees in aerospace engineering and the M.S. and Ph.D. degrees in electrical engineering from the University of Texas, Austin, in 1993, 1997, 1999, and 2001, respectively.

From 2004 to 2009, he held dual appointments as an Assistant Professor with the Department of Civil and Coastal Engineering and the Department of Electrical and Computer Engineering, University of Florida (UF), Gainesville. In 2009, he was granted tenure and promoted as an Associate Professor with the Department of Electrical and Computer Engineering, UF. His research interests included remote sensing applications of ALSM and InSAR, high-dimensional data segmentation, multiscale data fusion, graphical models, and photonics, with sponsored projects from the National Science Foundation (NSF), the National Aeronautics and Space Administration (NASA), the U.S. Army, the U.S. Navy, and the National Oceanic and Atmospheric Administration (NOAA). In 2010, he lost a 13-month battle with cancer, and the world lost a brilliant researcher, talented teacher, and loving husband and father.

Dr. Slatton was a recipient of the Presidential Early Career Award for Scientists and Engineers in 2006 for his work on predicting signal propagation in highly cluttered environments using remotely sensed geometry for ALSM.

**Tristan K. Cossio** (M'11) received the B.S., M.S., and Ph.D. degrees from the University of Florida (UF), Gainesville, in 2004, 2006, and 2009, respectively.

He is currently with the Johns Hopkins University Applied Physics Laboratory, Johns Hopkins University, Baltimore, MD. His research interests include remote sensing modeling and simulation, statistical signal processing, and target detection and classification.